1-1-2017

Using 210po/210pb Disequilibria To Characterize The Biogeochemistry And Quantify The Dynamics Of Sea Ice In The Arctic

Katherine Denise Krupp
Wayne State University,

USING $^{210}Po/^{210}Pb$ DISEQUILIBRIA TO CHARACTERIZE THE BIOGEOCHEMISTRY AND QUANTIFY THE DYNAMICS OF SEA ICE IN THE ARCTIC

by

KATHERINE KRUPP

THESIS

Submitted to the Graduate School

of Wayne State University,

Detroit, Michigan

in partial fulfillment of the requirements

for the degree of

MASTER OF SCIENCE

2017

MAJOR: GEOLOGY

Approved by:

M. Ba Tsaam 7/18/2017

Advisor Date

DEDICATION

To everyone who supported me during my time as a graduate student: thank you all.

ACKNOWLEDGEMENTS

I wish to thank my advisor, Mark Baskaran, and committee members Sarah Brownlee and Carol Miller for their guidance. I also thank John Niedermiller and Michele Blundell for their help with laboratory procedures. Furthermore, I thank Dave Kadko, Greg Cutter, Robert Anderson, and William Landing, the Chief and Co-Chiefs of the US GEOTRACES Expedition (respectively), as well as Tim Kenna and Martin Fleisher, of the Lamont-Doherty Earth Observatory, Columbia University, and Kyle Dilliplaine of the University of Alaska, Fairbanks, for their help with sample collection during the expedition. I also thank Aridane Gonzalez, of the Institut Universitaire Européen de la Mer for sharing samples from the German GEOTRACES Arctic expedition, and Matt Charette and Lauren Kipp of Woods Hole Oceanographic Institute for their contribution of data. This work was funded by the National Science Foundation (NSF Award Number: PLR-1434578).

TABLE OF CONTENTS

TABLE OF CONTENTS (CONTINUED)

TABLE OF CONTENTS (CONTINUED)

LIST OF TABLES

LIST OF FIGURES

CHAPTER 1

INTRODUCTION

Understanding the biogeochemical cycles of the world ocean is important to establish the mechanisms and factors influencing marine ecosystems, the dynamics of the global carbon budget, and the sources, sinks, and internal cycling of key nutrients and micronutrients (GEOTRACES 2006). This is expressly necessary in the Arctic Ocean, where 1) many characteristics that are unique to the Arctic Ocean have a significant impact on the biogeochemical cycling of important elements compared to in non-polar oceans, and 2) the effects of anthropogenic global change are particularly significant due to their effect on spatial and temporal Arctic sea ice extent and the global radiation balance. Unique to the Arctic are the expansive continental shelves which make up 36% of the ocean's surface area (e.g. Smith et al. 2003). The extensive shelf and slope regions are responsible for a greater recycling of nutrients, and are also able to remove contaminants from the water column through uptake by suspended particulates or by reaction with oxidized metals (e.g. Smith et al. 2003). Because sea ice is mainly formed in shallow (typically <20 m) coastal areas before drifting to deeper basins, nutrients and trace elements associated with the shelf sediments can be transported to the open ocean via ice-rafting (Nürnberg et al. 1994; Masqué et al. 2007; Trimble and Baskaran 2005). Sedimentary material can also be transported from the shelf to open waters through eddy transport and ventilation by dense bottom water (Lepore et al. 2009; Melling and Moore 1995; Pickart et al. 2005; Weingartner et al. 1998). Moreover, the Arctic receives a comparatively large amount of freshwater due to seasonal riverine input and meltwaters. Approximately 10% of the global riverine freshwater is discharged into the Arctic, which comprises only 1% of the global oceanic water volume (e.g. Trimble and Baskaran 2005). In addition to this input, seawater

brought into the Arctic Ocean via the Bering Strait (Pacific) and Fram Strait (Atlantic), as well as the salt rejection during ice formation in the surface ocean result in prominent stratification of the deep Arctic water column, producing four distinct water mass layers: the polar mixed layer (25 to >50 m depth in winter; 5 to 30 m depth in summer), the Atlantic/Pacific halocline (50 to 200 m depth), the Atlantic layer (below 300 m depth), and the Canada/Eurasian Basin bottom water (below 800 m depth) (Peralta-Ferriz and Woodgate 2015; Nguyen et al. 2009; Lepore et al. 2009; Aagaard et al. 1985; Schlosser et al. 1995). Furthermore, the areal extent of permanent and seasonal ice coverage is variable, resulting in variable distribution of bio- and lithogenic particle distribution. In general, the inventory of suspended particulate matter is 1 to 2 orders of magnitude lower in areas covered by permanent ice than by seasonal ice (7.3 g m^{-2} versus 76-92 g m^{-2}, respectively, integrated over a 1500 m water depth) (Bacon et al. 1989; Baskaran et al. 2003; Trimble et al. 2004). Finally, biological activity is highly dynamic in the Arctic due to extended periods of time both with sunlight (Arctic summers), and without sunlight (Arctic winters), which leads to extreme spatial and seasonal changes in primary productivity (Trimble and Baskaran 2005; Lepore et al. 2009). In summary, the factors that the concentrations, cycling, and transport of trace metals, contaminants, and nutrients, as well as water mass transport in the Arctic can be markedly different from other oceans (Smith et al. 2003).

The measurements of ^{210}Po and ^{210}Pb in aerosols, seawater, and organic and inorganic particulates have been used extensively in oceanographic research to determine residence times, scavenging intensity, particulate organic carbon (POC) export flux, carbon remineralization depths, shelf-basin transport and sediment focusing, and to understand the distribution of essential particle-reactive trace metals and micronutrients such as iron, lead, and zinc (e.g., Baskaran 2011; Verdeny et al. 2009; Lepore et al. 2009; Rigaud et al. 2015). Polonium-210

($t_{1/2}$=138.4d) and lead-210 ($t_{1/2}$=22.3y) are a parent-granddaughter pair (separated by the short-lived ^{210}Bi ($t_{1/2}$=5.012d)) within the uranium-238 decay series. Uranium-238 ($t_{1/2}$=4.5 x 10^9y), a ubiquitous element in the Earth's crust, decays to stable ^{206}Pb through a number of radioactive isotopes, including ^{222}Rn ($t_{1/2}$=3.8d), an inert noble gas. A fraction of this ^{222}Rn produced in rocks, minerals, soils, and surface waters escapes to the atmosphere. Atmospheric ^{222}Rn then decays to ^{210}Pb through a series of short-lived intermediates. The residence time of ^{210}Pb in the troposphere averages about 10 days, and thus most ^{210}Pb is deposited back onto Earth's surface and onto surface waters via wet (and to a lesser extent, dry) deposition (e.g. Semertzidou et al. 2016; Matisoff and Whiting 2011). Atmospherically-deposited ^{210}Pb decays to the short-lived ^{210}Bi, and then to ^{210}Po. This isotopic pair is useful for tracing environmental processes for three key reasons: 1) they are naturally-occurring, 2) due to their known half-lives and timescale of incorporation, they can be used to quantify time-dependent parameters including residence times, transport rates, and mass fluxes, and 3) they are particle-reactive and can therefore be used to trace the behavior of other particle-reactive trace elements and contaminants (e.g. Verdeny et al. 2009). The ^{210}Po/^{210}Pb activity ratio is especially suited to trace the cycling of carbon in seawater due to the preferential adsorption and assimilation of ^{210}Po to organic particles relative to ^{210}Pb (e.g. Verdeny et al. 2009). This departure from secular equilibrium (referred to here as ^{210}Po/^{210}Pb disequilibrium) provides a means to characterize the biogeochemistry of the ocean on sub-annual time scales (weeks to months) (Verdeny et al. 2009; Murray et al. 2005; Stewart et al. 2007; Hong et al. 2013).

With a mean life of 200 days, the timescale of utility of the ^{210}Po-^{210}Pb pair is on the order of months, making it useful to study seasonal ice floe dynamics. The residence time, thickness, and areal extent of sea ice all affect the radiation balance of the Arctic (Nürnberg et al.

1994; Aagaard et al. 1985; Clark 1990). The main factor which dictates the effects of solar insolation is the differing surface albedo of open water, ice, and sea-ice sediments (Tucker et al. 1999). Tucker et al. (1999) have reported the integrated albedo of fresh snow to be 0.83, and of multiyear ice floes to be 0.71. In contrast, algae or sediment-laden ice had a far lower integrated albedo of 0.48, and melt pond albedos ranged from 0.1 to 0.3 (e.g. Tucker et al. 1999). During Arctic winters, when sea ice extent is at a maximum, approximately 80% of solar radiation is reflected, thereby regulating the temperature of the region (National Snow and Ice Data Center, n.d.). Arctic sea ice is reduced by melting in the summers, which reduces the overall albedo of the ocean, thereby increasing melt and further decreasing albedo in a positive-feedback scenario (Tucker et al. 1999; Kellogg 1975; Moritz and Perovich 1996). A small increase in global temperature due to anthropogenic climate change could further amplify this effect (National Snow and Ice Data Center, n.d.). This study introduces a novel approach to constrain the residence time of ice-rafted sediment (IRS) and rate of sea ice formation/ablation using $^{210}Po/^{210}Pb$ disequilibria.

1.1 Summary of previous work

The study of ^{210}Po and ^{210}Pb disequilibria has been applied to the biogeochemical characterization of both the shelf/slope regions and interior basins of the Arctic (Figure 1). Both the dynamic biological activity and large difference in particulate concentration, composition, and flux, result in highly variable scavenging of ^{210}Po and ^{210}Pb by particles in different regions of the Arctic. Particle concentrations are generally greater in the shelf region compared to the interior basin (30 μg L^{-1} – 1000 μg L^{-1} versus ~5 μg L^{-1}, respectively), though suspended particulate matter has been observed to vary over an order of magnitude within deep Arctic basins as well (from 7.3 to 90.8 g m^{-2} integrated over 1500 m depth) (Lepore et al. 2009; Bacon

et al. 1989; Stein and Macdonald 2004; Trimble et al. 2004). Within the Canada basin, suspended particulate matter concentrations have been found to vary from 29 to 1054 μg L^{-1}, with higher concentrations observed in coastal regions (Trimble and Baskaran 2005). Particulate residence time in the Canada basin ranges from 4.8 to 151 days (7 ± 1 days in surface waters) (Trimble and Baskaran 2005; Baskaran et al. 2003). Lead-210 has a stronger affinity to lithogenic particles compared to biogenic particles, therefore, dissolved ^{210}Pb concentrations in the water column are affected by sedimentary particle distributions, and specifically by removal via scavenging at ocean margins. In contrast, the residence time of ^{210}Po is primarily affected by biogenic particle scavenging in areas of greater productivity. Because an estimated 85% of biological activity in the Arctic occurs in its expansive continental shelves, these regions are a significant source of particulate organic carbon (POC) to the interior basin (Lepore et al. 2007; Moran et al. 2005; Lepore et al. 2009). However, sea ice algae production in the central Arctic Ocean can also contribute significantly to total annual primary productivity (up to 52%) (e.g. Trimble and Baskaran 2005). As a result of these variable particle concentrations and residence times, it is expected and has been reported that the residence times of the particle-reactive ^{210}Po and ^{210}Pb are variable in the Arctic as well. Moore and Smith (1986) observed ^{210}Pb scavenging by continental margins, resulting in a comparative ^{210}Pb deficit (relative to ^{226}Ra) in the interior basins of the Arctic. Scavenging from continental margins was also observed by Smith et al. (2003), who compared ^{210}Pb in water columns to sediments in the Western and Central Arctic and reported a net scavenging of ^{210}Pb, with an observed deficit in the Makarov and Canada basins. Also observed were elevated dissolved ^{210}Po and ^{210}Pb activities in nutrient maximum surface waters of coastal stations relative to interior stations, which the authors attributed to the lateral advection of ^{226}Ra, a parent isotope of ^{210}Pb, with upper halocline water. Lepore et al.

(2009) observed the removal of ^{210}Pb in the Chukchi Sea by resuspended sedimentary particles (with excess ^{210}Pb inventory ranging from 7.69 to 85.10 dpm cm^{-2}), along with low ^{210}Pb in the halocline of the Canada Basin, which was attributed to shelf scavenging and subsequent advective transport to the deep basin. An observed dissolved ^{210}Pb minimum in the Canada Basin corresponds to the halocline layer which is transported from the shelf to interior in the Western Arctic by mesoscale eddy transport or seasonal outflow, and has been independently observed by many aforementioned studies (Lepore et al. 2009; Moore and Smith 1986; Smith and Ellis 1995; Smith et al. 2003). In summary, numerous previous studies have confirmed the variable scavenging of particle-reactive radionuclides, primarily due to the characteristics of the expansive continental shelf region of the Arctic and its effect on particle distribution and composition.

Another influence on ^{210}Po and ^{210}Pb disequilibria is the spatial and temporal extent of Arctic sea ice. Due to its direct relationship with solar energy absorption, sea ice affects primary productivity and thus vertical particle flux from surface waters. During summer months, POC export flux is spatially heterogeneous, with higher fluxes observed in shelf regions relative to deep basins (>30 mmol m^{-2} d^{-1} in the shelf versus <5 mmol m^{-2} d^{-1} in deep basins) (Cochran et al. 1995; Lepore et al. 2007; Moran et al. 1997; Cai et al. 2010; Roca-Marti et al. 2016). In 2012, a ^{210}Po deficiency in the upper water column (to depths of 150 to 190 m) of the central Arctic was observed, with ^{210}Po/^{210}Pb ratios as low as 0.21 ± 0.12 (Roca-Marti et al. 2016). This deficiency coincided with high concentrations of seafloor algae coverage, indicating that ^{210}Po was assimilated into algal material and exported with sinking biogenic particles during the early summer months (Roca-Marti et al. 2016). The ^{210}Po/^{210}Pb activity ratios published in this study

are similar to the activity ratios found at high latitude stations sampled in 1994, which were as low as 0.22 ± 0.10 (Smith et al. 2003).

While only a handful of studies on ^{210}Po and ^{210}Pb disequilibria in the Arctic Ocean have been conducted, even fewer have focused on the sea ice itself. In this study, we assert that sea ice extent and ice floe dynamics can be studied directly by measuring this radionuclide pair in sea ice, snow, melt pond waters, and ice-rafted sediments. Baskaran (2005) quantified the activity of ^{210}Pb in ice-rafted sediments of the western and central Arctic, concluding that excess ^{210}Pb was commonly present in IRS sediments due to enrichment by meltwaters from snow/ice and surface waters. The transit times of sea-ice sediments and ice floes in the Arctic have also been quantified through the use of ^{7}Be/^{210}Pb$_{excess}$ activity ratios (Masqué et al. 2007). Vertical activity ratios in Arctic ice cores were measured in one study prior to this study, but the ratios were in equilibrium within their uncertainties throughout the total length of the core, prohibiting the ability to obtain any useful time information (Masqué et al. 2007). This study provides ^{210}Po and ^{210}Pb measurements for the first time for melt pond, snow, and under ice seawater.

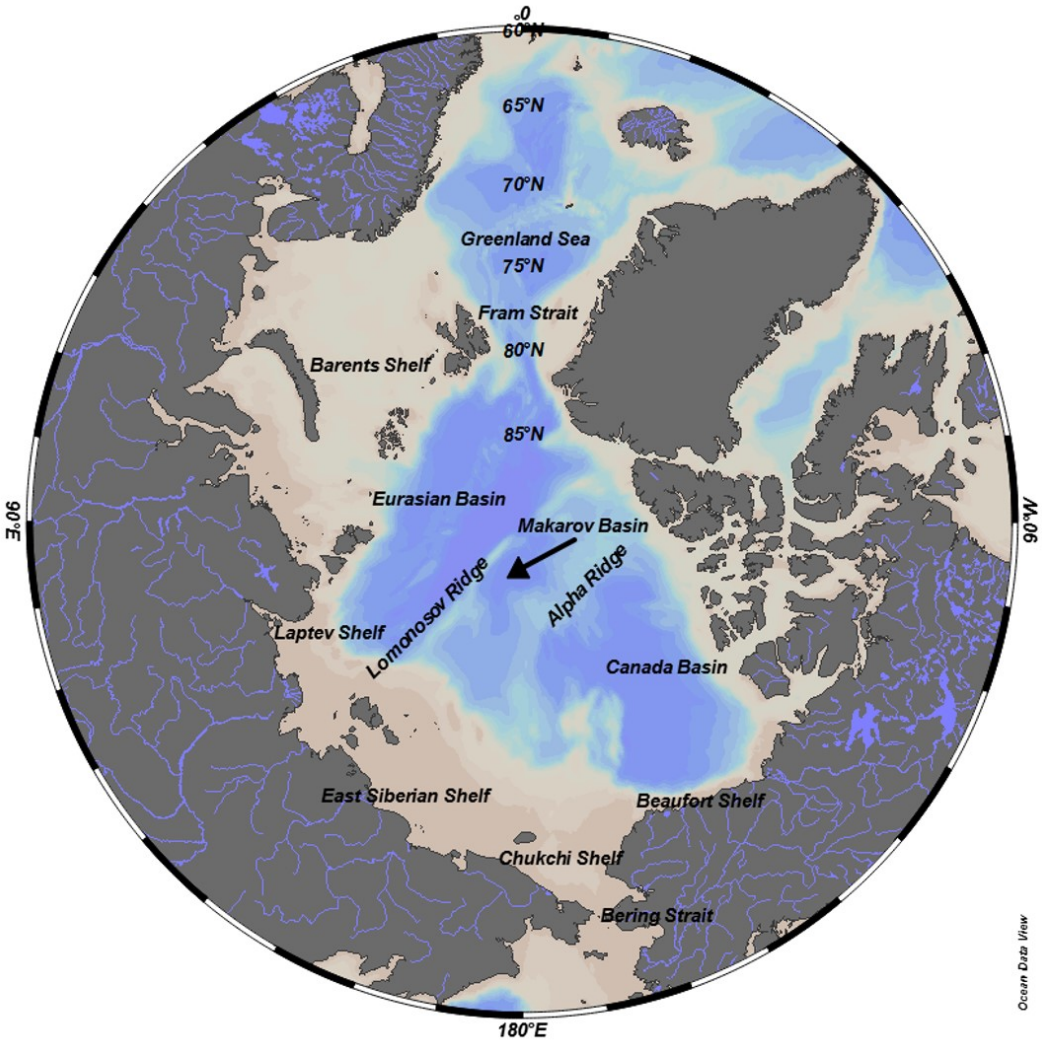

Figure 1. Major ridge, shelf, and basin regions of the Western and Central Arctic Ocean.

1.2 Objectives

1.2.1 Constraining IRS residence times in the Arctic

One of the objectives of this study is to constrain the residence time of ice-rafted sediments (IRS) in the Arctic using the in-growth time of ^{210}Po towards secular equilibrium with its grandparent, ^{210}Pb. This in-growth is measured from the time of incorporation of ^{210}Po and ^{210}Pb by atmospheric deposition, thus providing the duration of time that the IRS was incorporated into surface ice. The primary way in which IRS is formed is through the incorporation of suspended sediments of terrigenous origin into frazil ice in the coastal areas of

the Arctic Ocean (Nürnberg et al. 1994; Eicken et al. 1997). Secondary processes include the incorporation of benthic sediments into anchor ice which is subsequently uplifted, and the transport of riverine sediments in coastal regions (Eicken et al. 1997). Incorporation of Aeolian dust into sea ice has also been proposed, though its input is relatively insignificant, with deposition rates of airborne dust in the region ranging from 3.3-14.0 μg cm^{-2} y^{-1} (Cooper et al. 1998; Darby et al. 1974). Frazil ice (suspended pieces of ice crystals; the first stage in the formation of sea ice) form in coastal, turbulent waters and marginal ice zones, where suspended sediments are present in higher concentrations than in the interior basin. The successive accumulation and assemblage of frazil ice due to decreased temperatures forms ice sheets, which can break from the shelf and drift into the interior basin of the Arctic, thus allowing the transport of sediments and associated materials. The main sources of IRS are the coastal waters of the Siberian shelves and the Laptev Sea (having seawater depths of <50m), with annual IRS export estimates ranging from 2 to 150 x 10^6 tons (where export refers to the transport of IRS from the Arctic shelf regions to the North Atlantic, through the Fram Strait) (Dethleff 2005; Masqué et al. 2007). Other reports have indicated that discoloration by bio- and lithogenic particles covers 10 to 50% of the Arctic ice pack (Pfirman et al 1995; Pfirman et al. 1990; Nürnberg et al. 1994). The composition of IRS is mainly clay minerals with silt and sand components, however, the presence of larger grain sizes (up to gravel-sized) have been found (Eicken et al. 1997; Cooper et al. 1998; Nürnberg et al. 1994; Tucker et al. 1999). Constraining the "age" of these IRS is significant because 1) IRS transport is not yet well understood due to compromised visibility of sea-ice sediments via satellite imagery in Arctic winters 2) even minor contributions of particulate matter can have a great effect on the deep Arctic basins due to their lower concentrations in the deep Arctic basins, and 3) atmospheric deposition of pollutants from Arctic

haze can eventually be incorporated into IRS and transported long distances across the Arctic and into the North Atlantic (Tucker et al. 1999; Lepore et al. 2009; Cooper et al. 1998; Pfirman et al. 1995; Baskaran 2005).

1.2.2. Quantifying ice floe dynamics

The second objective of this study is to estimate the accumulation and ablation rate of Arctic ice sheets using measured $^{210}Po/^{210}Pb$ activity ratios collected from aerosol, snow, ice core, melt pond, and "under-ice seawater" (surface water below ice sheet) samples. The areal extent and thickness of Arctic sea ice varies seasonally, with the sea ice maximum occurring in late February or March, and the sea ice minimum occurring in September. The established sea ice maximum in 2015 occurred on February 25, with an area of 14.54×10^6 km^2, and its minimum occurred on September 11, 2015, with the area dropping to 4.41×10^6 km^2 (National Snow and Ice Data Center n.d.). Approximately 30% of ice is multiyear ice, which persists through the melt season (National Snow and Ice Data Center n.d.). Melt ponds, which are pools of freshwater that collect on or under sea ice, are a feature of the melt season. Polonium-210 and ^{210}Pb in sea ice, melt ponds, and snow, which covers sea ice for most of the year, are derived from atmospheric deposition. The quantification of ice accumulation and ablation rates is of great significance due to their role in the summer ice budget, and thus their contribution to the overall understanding of the Arctic radiation balance. In order to quantify these rates, the variations in the $^{210}Po/^{210}Pb$ activity ratio (AR) will be utilized, with the following assumptions: 1) the initial $^{210}Po/^{210}Pb$ AR is introduced to the Arctic ocean surface by atmospheric deposition and is constant, 2) ice floe accumulation is dominated by the formation of ice via compacted snow and the time elapsed between the deposition of snow and snow becoming ice is short

compared to the mean life of ^{210}Po, and 3) ice melts primarily from the bottom layer of sea ice based on the principle of hydrostatic equilibrium. Detailed models are presented in section 3.2.

1.2.3 Distribution and applications of ^{210}Po and ^{210}Pb in seawater

The third objective is to measure the vertical profiles of particulate and dissolved activities of ^{210}Po and ^{210}Pb in the central Arctic Ocean in order to: 1) investigate the processes that control fractionation between ^{210}Po and ^{210}Pb and remineralization of particulate ^{210}Po and ^{210}Pb at different depths, 2) determine zones of enhanced scavenging of these nuclides by suspended particles in the water column, 3) determine the flux of ^{210}Po and ^{210}Pb in the water column and, by proxy, the flux of important particle-reactive trace elements (including Fe, stable Pb, and Zn), and 4) quantify the export flux of particulate organic carbon (POC) and characterize the biological pump in Arctic surface waters using POC data in conjunction with other isotopic data. It is hypothesized that changes in sea ice-extent may affect net primary productivity, in turn affecting ^{210}Po deficiency in the water column. Activity ratios will be examined in both the Makarov Basin at a station near the Alpha Ridge. In addition, published data from the Alpha Ridge and other stations in the Western and Central Arctic Ocean will be utilized for comparison of the magnitude of ^{210}Po and/or ^{210}Pb deficiency and possible causes. Previous studies on the vertical profiles of ^{230}Th have reported contrasting residence times in different basins of the Arctic, where longer residence times were reported in the Makarov basin. Since ^{210}Pb behaves similarly to ^{230}Th, the present study will be able to assess if the residence time of ^{210}Pb is also longer in the Makarov Basin compared to the other basins in the Arctic Ocean. Lead-210 residence times in the Makarov Basin versus Alpha Ridge will be compared to test this hypothesis. This dataset will also be compared with previous studies to determine any differences in radionuclide inventory and scavenging intensity in the deep basins of the Arctic.

Finally, a comparison of these activities in the deep basins versus the shelf waters of the Chukchi Sea will provide insight on the boundary scavenging of ^{210}Pb, which will complement previous reports. It is hypothesized that ^{210}Po and ^{210}Pb will vary for different basins in the Arctic due to changes in scavenging intensity due to variable particle concentrations and biogenic activity, as well as the difference in the depositional flux of ^{210}Pb with latitude. This last item will be performed in future collaboration with participating US GEOTRACES scientists, and is therefore not included in this thesis.

CHAPTER 2

MATERIALS AND METHODS

The samples analyzed for in-situ ^{210}Po and ^{210}Pb were collected from eleven different stations along a transect through the Western and Central Arctic Ocean (Figure 2). Of these stations, ice-rafted sediments were collected from two stations (E-6195 and -6244), water profiles were sampled at two 'super stations' (a station is considered a super station when water columns were sampled at high resolution for a full suite of analytes, including trace elements and isotopes) (ST-30 and -43), and six stations were 'ice stations' where ice cores, melt pond, snow, and under ice samples were collected (ST-31, -33, -39, -42, -43 and -46) (note that ST-43 shared a super station and ice station). An additional set of ice-rafted sediment samples (n=6) were collected from two stations by the German GEOTRACES expedition and sent to the Wayne State laboratory for analysis (GERIRS 1 and GERIRS 2). Furthermore, fourteen aerosol deployments were conducted using a large-volume aerosol collection system during the cruise, where each deployment averaged 30 hours of run time and an aliquot of the aerosol filter (equivalent to ~ 180 m^3 of filtered air) was provided to us (Figure 2). Table 1 lists the number of samples collected for each sample type. Additional shelf and slope stations, as well as two super stations in the Canada basin and marginal ice zone were analyzed for ^{210}Po/^{210}Pb by a collaborating group and are not included in this study, but two samples were collected for each group for inter-calibration purposes. An intercalibration of the ^{209}Po spike used in our laboratory with that of our collaborator at Louisiana State University was also conducted.

Table 1. Comprehensive list of samples collected on US GEOTRACES Western Arctic expedition, aboard the USCGC Healy (WAGB-20) from August 9 – October 12, 2015 (GEOTRACES Cruise number: HLY1502).

Sample Type	Number of Samples (dissolved/particulate)
Water column	117 (40/77)
Aerosol	14
Ice Core	62 (31/31)
Melt Pond	10 (5/5)
Snow	12 (6/6)
Under Ice Seawater	12 (6/6)
IRS	12
Surface seawater (for inter-calibration)	2

To investigate the partitioning of ^{210}Pb and ^{210}Po, all seawater and sea ice samples were filtered into dissolved and particulate fractions for separate analyses (Figure 3). Dissolved water column samples were collected using Niskin bottles attached to a CTD rosette and cast at designated depths for each station. Upon collection, 20 L samples were filtered with 0.4 µm Acropak filter capsules, transferred into acid-washed polyethylene cubitainers, and acidified to a pH of 2 using 60 mL of 6M Omni-trace hydrochloric acid. Acidifying the samples minimizes the potential loss of ^{210}Po or ^{210}Pb due to leaching by the storage container walls, and prepares the samples for pre-concentration chemistry (Baskaran et al. 2013). The corresponding small (<51 µm) and large (>51 µm) particulate fractions were collected using modified dual-flowpath battery-powered McLane in-situ pumps, which were cast at each station to match the depth-resolution of the dissolved water column samples. The pumps filtered an average of 160 L of water through quartz microfiber (QMA) filters for each sample. Once collected, filters were dried at room temperature under a HEPA-filtered hood. A series of dip blanks were also collected for each station to assess the amount of passive sorption of ^{210}Po and ^{210}Pb onto the QMA filters (Church et al. 2012).

At ice stations, 20 L unfiltered melt pond and under ice samples were collected into carboys and filtered in the onboard laboratory using 0.4 µm Whatman Nuclepore track-etched membrane filters and a vacuum filtration system. Snow samples were collected into two 20 L cubitainer bags and melted to a volume of 20 L, then filtered. Two ice cores were taken at each station, evenly divided into segments (typically 5 segments ranging from approximately 20-40 cm each), combined, and melted before filtering in the same manner. All filters were retained for particulate analysis, and filtered water samples were acidified to a pH of 2 with 6M HCl. Last, the ice-rafted sediments were collected by shoveling sediment-laden ice fragments into 20 L buckets. These samples were melted, sediments were allowed to settle, and the 'supernatant' meltwater was poured off to concentrate the sample. The sediment solution was then dried in an oven at 100°C and leached using particulate sample protocols.

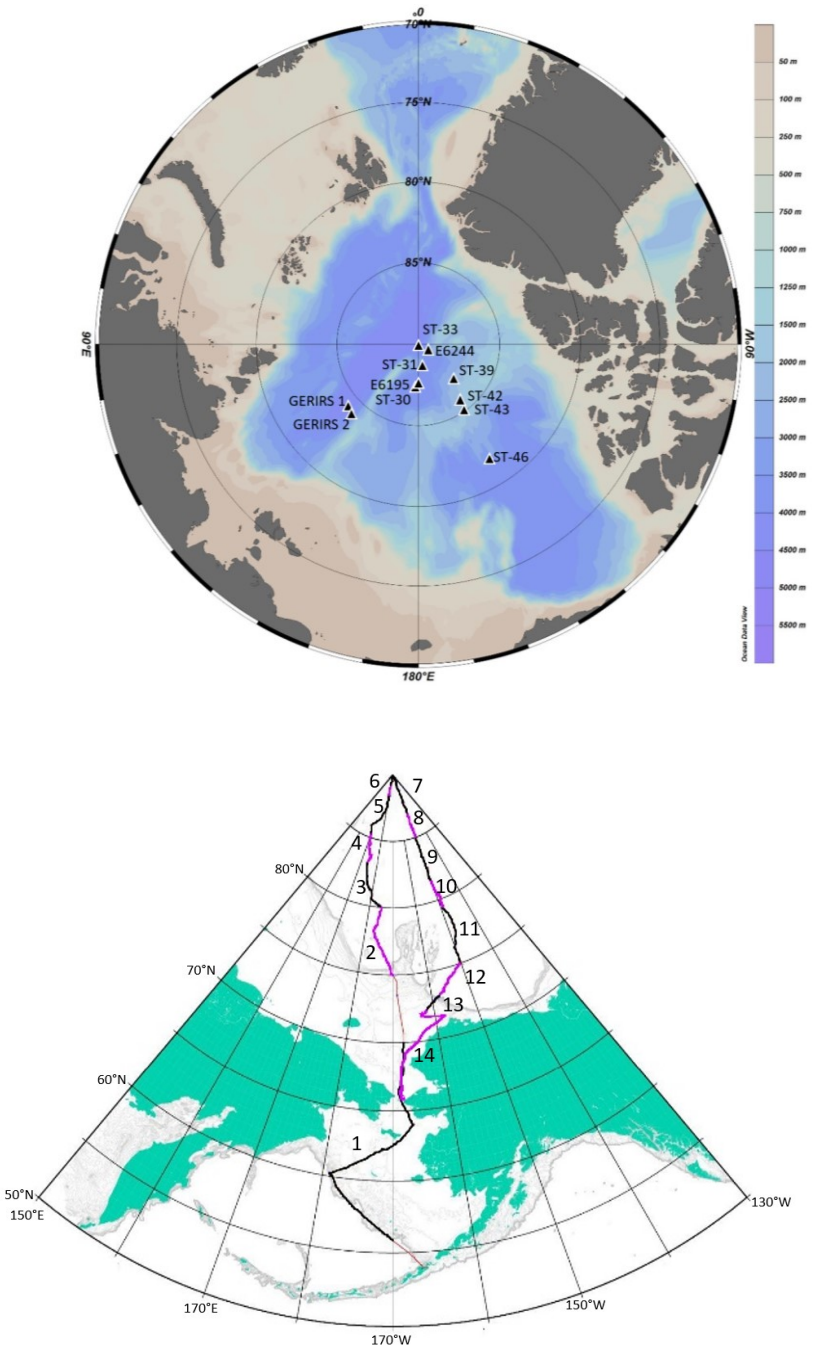

Figure 2. Full station map (top) and aerosol deployment map (bottom). Aerosol deployment map is adapted from U.S. GEOTRACES Cruise Report (2015).

2.1 Determination of in-situ ^{210}Po activity

2.1.1 Dissolved fraction analysis

To measure the amount of ^{210}Po in dissolved samples, a ferric hydroxide co-precipitation method was first performed for the pre-concentration of the isotopes of interest. The protocol used was based on the process detailed in the Sampling and Sample-handling Protocols for GEOTRACES Cruises (known as *'Cookbook'*) (Cutter et al. 2010; http://www.geotraces.org/science/intercalibration/222-sampling-and-sample-handling-protocols-for-geotraces-cruises). Upon acidification, each sample was spiked with 1) a known amount of ^{209}Po US-NIST Standard Reference Material as an internal yield tracer, 2) 20 mg of stable lead via a stable lead carrier of $PbCl_2$ in order to calculate chemical efficiency of ^{210}Pb recovery, and 3) an iron carrier ($FeCl_3$; 5 mg Fe/L of water) to co-precipitate ^{210}Po and ^{210}Pb with $Fe(OH)_3$ precipitate. Due to the inability to accurately weigh materials on the ship, the spikes were measured out using a carefully calibrated volumetric pipette. After a 12-24 hour equilibration period, ammonium hydroxide was added to samples to increase the pH from 2 to 4, and then 1 mL of 10% sodium chromate was added to increase the lead yield by the co-precipitation of lead chromate. Then the pH was increased to ~8. This rise in pH causes the iron to flocculate to co-precipitate ^{210}Po and ^{210}Pb with $Fe(OH)_3$. After successive decanting, pumping off supernatant, and filtration to separate precipitate from solution, the precipitate was dissolved with 5 ml 6M Omni-trace HCl and collected into a Teflon beaker. An additional 35 ml of deionized water was used to rinse the filter paper and increase the total volume to 40 ml and pH of the concentrated sample solution to approximately 0.8. In order to prevent iron compounds from interfering with ^{210}Po electroplating, ~200 mg of ascorbic acid was then added to the solution to reduce Fe^{3+} to Fe^{2+}. A polished silver planchet with one side taped was then placed at the bottom of the beaker

containing the solution. The solution was stirred with a magnetic stirrer bar for 24 hours at room temperature in order to deposit ^{210}Po from the solution by spontaneous electroplating. After plating, each solution was stored in a precleaned 60 ml Nalgene bottle and stored for further onshore ^{210}Pb analysis. The planchets were counted for ^{209}Po and ^{210}Po via alpha spectrometry.

2.1.2 Particulate fraction analysis

All particulate sample processing was performed using leaching methods developed based on experiments detailed in section 2.4. The aerosol samples (PM 10 filter) as well as ice station samples (0.4 µm Whatman filters) were leached with 10 mL 6M Omni-trace HCl and 10 mL 8M Omni-trace HNO3 in a 50 ml centrifuge tube and agitated for one hour at 70°C in an ultrasonic bath. These solutions were then filtered, spiked with a known amount of ^{209}Po and stable Pb, dried, diluted to 40 ml with deionized water, and then the solution was used for electroplating. The particulate samples (>51 µm, 1-51 µm) collected from McLane pumps were processed at the Wayne State laboratory after the expedition concluded, and followed a similar procedure, with the exception that digestion vessels were used in place of an ultrasonic bath. After electroplating, each sample solution was stored for further processing and ^{210}Pb analysis.

2.2 Determination of in-situ ^{210}Pb activity

After polonium plating, any residual ^{210}Po (and ^{209}Po) must be removed from sample solutions for the future measurement of ^{210}Pb, which is measured by the in-growth of ^{210}Po from the decay of ^{210}Pb. The quantitative removal of ^{210}Po was performed by a column separation technique, where samples were first evaporated, then taken into a 9M HCl solution and passed through a 9M HCl pre-conditioned anion-exchange column (DOWEX 1X8, chloride form, 100-200 mesh). The eluted solution was spiked with a known amount of ^{209}Po yield tracer and stored in a pre-cleaned 100 ml plastic bottle until sufficient in-growth of ^{210}Po occurred (>6-12

months). In order to determine the time at which in-growth was sufficient for second plating (i.e. will produce low counting errors), Equation 1 was used:

$$A(^{210}Po) = A(^{210}Pb)*(1-e^{-\lambda t}) \quad \text{Eq (1)}$$

where t is the time elapsed between the column separation and second plating of ^{210}Po. The calculated ^{210}Pb activity was converted to counts per ten days. Any resultant number higher than 1000 counts per ten days is considered adequate for plating, as this yields an error of 3% or less. In order to quantify ^{210}Pb recovery, a 5% aliquot was taken from each sample after column separation and measured for stable lead by ICP-MS (see section 2.3).

After an in-growth period of 6-12 months, samples were transferred to Teflon beakers and reduced to <5 ml, then diluted to 40 ml using distilled water. In the first batch of samples, an unknown residue was observed on the plated Ag disks which affected the resolution of the alpha energy peaks of the first sample set plated (ice-rafted sediments, and snow from station 31) resulting in high count errors (~25-70%). These planchets were leached in a warm (~80°C) 6M HCl bath for ~60 minutes to remove the impurities from the surface. The planchets were then recounted and the resolution of the peak improved drastically. The count rate in the leachates of impurities were found to be ~1% of the total counts for both the ^{210}Po and yield tracer (^{209}Po). This residue was not present on subsequent samples and no planchet cleaning was required.

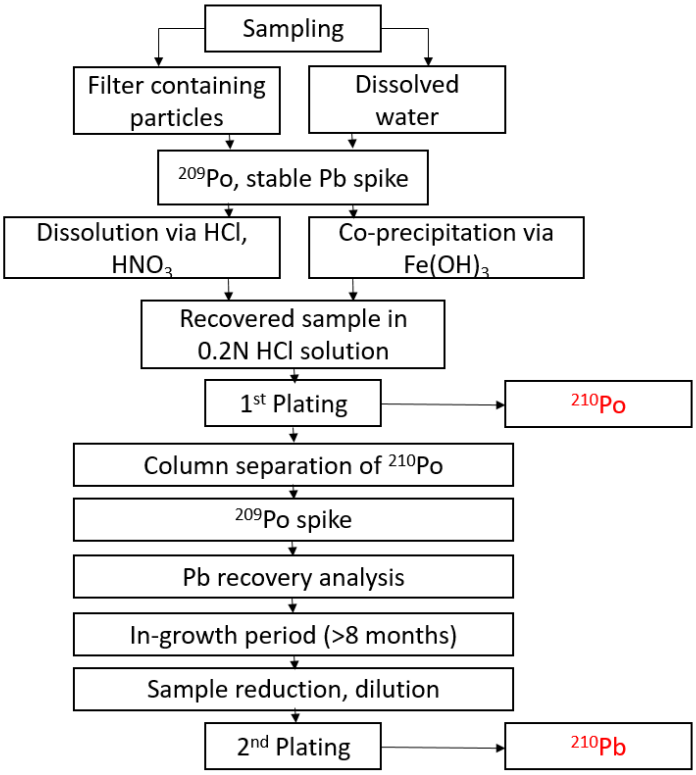

Figure 3. Processing protocol flow chart (adapted from Church et al. 2012).

2.3 Governing equations in the calculation of final activities of ^{210}Po and ^{210}Pb

The ^{210}Po count rates assayed by alpha spectrometry must first be corrected for the background activity of each sample's respective detector. Next, due to the relatively short half-life of ^{210}Po (138.4 days), the measured activity in each sample requires a series of corrections for the decay and/or in-growth of both ^{210}Po and ^{210}Pb. The in-situ ^{210}Po activity must be corrected to account for 1) the decay of ^{210}Po from the time of collection to the time of first plating, which results in an underestimate of the in-situ activity, and 2) the ingrowth of ^{210}Po via ^{210}Pb from the time of collection to the time of first plating, which results in an overestimate of the in-situ activity. The in-situ activity of ^{210}Po is calculated by Equation 2 (Baskaran et al. 2013):

$$A^{\text{Po-210}}{}_{\textit{in-situ}}\ (\text{dpm}) = [A'_{\text{Po-210}} - A_{\text{in-growth}}]e^{-\lambda_{\text{Po-210}}T} \qquad \text{Eq (2)}$$

where T is the elapsed time between collection and first plating, $\lambda_{Po\text{-}210}$ is the decay constant of ^{210}Po, and $A'_{Po\text{-}210}$ and $A_{in\text{-}growth}$ are given by Equations 3 and 4, respectively (Baskaran et al. 2013):

$$A'_{Po\text{-}210}\,(dpm) = (^{210}N/^{209}N)e^{\lambda_{Po\text{-}210}t_1}\,A_{spike} \qquad \text{Eq (3)}$$

where ^{210}N and ^{209}N are the background subtracted counts of ^{210}Po and ^{209}Po, respectively, t_1 is the time elapsed from first plating to mid-counting, and A_{spike} is the activity of the ^{209}Po spike. This term applies the use of ^{209}Po as a measure of chemical efficiency.

$$A_{in\text{-}growth}\,(dpm) = A^{Pb\text{-}210}{}_{in\ situ}\,[\lambda_{Bi}\,\lambda_{Po}\,e^{-\lambda PbT}/(\lambda_{Bi}-\lambda_{Pb})(\lambda_{Po}-\lambda_{Pb}) + \lambda_{Bi}\,\lambda_{Po}\,e^{-\lambda BiT}/(\lambda_{Pb}-\lambda_{Bi})(\lambda_{Po}-\lambda_{Bi}) + \lambda_{Bi}\lambda_{Po}\,e^{-\lambda PoT}/(\lambda_{Pb}-\lambda_{Po})(\lambda_{Bi}-\lambda_{Po})] \qquad \text{Eq (4)}$$

where $A^{Pb\text{-}210}{}_{in\ situ}$ is the corrected in-situ activity of ^{210}Pb (discussed below), and λ_{Bi}, λ_{Po}, and λ_{Pb} are the decay constants of ^{210}Bi, ^{210}Po, and ^{210}Pb, respectively. Equation 4 is an application of Bateman's equation, which is a standard equation to determine the activity of a daughter product when its parent as well as its daughter simultaneously undergo radioactive decay (Faure and Mensing 2005). An additional term of $e^{-\lambda Po\text{-}209t2}$ may be multiplied to the terms on the right side of Equation 3 to account for the potential decay of ^{209}Po in the spike used. In this term, λ_{Po}-209 is the decay constant for ^{209}Po, and t_2 is the time from standard calibration to first plating. Due to the half-life of ^{209}Po (125 years) and short t_2 in this experiment (~30-90 days), this term was omitted in the first plating calculations, as it is approximately equivalent to 1 (0.9995 to 0.9985). However, this decay correction was included in the in-situ ^{210}Pb calculations due to the longer time from spike assay to plating.

The calculation of in-situ ^{210}Pb requires the correction for 1) the decay of ^{210}Po from second plating to mid-counting, which results in an underestimate of the in-situ activity, and 2)

the decay of ^{210}Pb from the time of collection to second plating, and is given by Equation 5 (Baskaran et al. 2013):

$$A^{Pb\text{-}210}_{\ in\ situ}\ (dpm) = A^{m}_{\ Po\text{-}210}\ e^{\lambda Pbt_6}/\eta_c[1-e^{-\lambda Pot_5}] \quad \text{Eq (5)}$$

where t_6 is the elapsed time between collection and second plating, t_5 is the time between ^{210}Po extraction and second plating, η_c is the chemical yield of ^{210}Po based on ICP-MS assay of stable Pb (= stable Pb assayed/stable Pb added to sample), and $A^{m}_{\ Po\text{-}210}$ is given by Equation 6 (Baskaran et al. 2013):

$$A^{m}_{\ Po\text{-}210}\ (dpm) = (^{210}N/^{209}N)e^{\lambda}_{Po\text{-}210}{}^{t}_{3}\ A_{spike} \quad \text{Eq (6)}$$

where ^{210}N and ^{209}N are the background subtracted counts of ^{210}Po and ^{209}Po, respectively, for the second plating, Aspike is the amount of ^{209}Po added, and t_3 is the time elapsed from second plating to mid-counting.

2.4 Pre-cruise optimization of chemical procedures

In preparation for the Arctic GEOTRACES research expedition (August 9 – October 12, 2015), experiments were performed to determine the relative efficiency of different methods for extracting polonium-210 from aerosol filters. These filters were generally digested completely using concentrated hydrochloric acid, nitric acid, and hydrofluoric acid, followed by drying, and then taken into dilute HCl solution for electroplating. In order to avoid usage of concentrated hydrofluoric acid on the cruise, we devised a series of different leaching procedures on aerosol filters (aerosol samples collected at Wayne State University campus) by both leaching and total digestion, and compared the amount of polonium-210 extracted by each method performed on separate aliquots of the same filter. Each 8 x 10 aerosol filter was filtered at a flow rate of 1.4m^3/minute for approximately 24 hours, such that the total volume of air filtered by each reported sample was 422 m^3. To leach the filters, varying concentrations of hydrochloric and

nitric acid (Table 2) were used. The filter samples were taken in a centrifuge tube and placed in an ultrasonic bath at 70ºC (details on volumes and concentration of acids used given in Table 2). The filtrate was then separated from each filter by vacuum filtration and the process was repeated once more.

The calculated ^{210}Po activities are tabulated in Table 2. We have found that leaching the filter with 6M hydrochloric acid and 8M nitric acid, followed by drying (necessary to prevent dissolution of planchet) and dilution, provides results consistent with total digestion with HF (^{210}Po = 0.329 ± 0.013 dpm/100 m^3 versus 0.315 ± 0.013 dpm/100 m^3 for leaching and digestion, respectively). The results show that 6M hydrochloric acid leaching alone is not efficient (^{210}Po = 0.250 ± 0.009 dpm/100 m^3), suggesting that nitric acid is necessary as an oxidizing agent to quantitatively extract polonium-210 from the aerosol filter due to possible presence of organic aerosol particles. These results also suggest that the complete destruction of the quartz microfibers by hydrofluoric acid is not necessary to extract polonium-210 from the filter media. This leaching method was used in place of total digestion on the cruise in order to eliminate the need for hydrofluoric acid and concentrated nitric and hydrochloric acid, as well as reduce the time usually needed to digest the aerosol filters, which is important when considering the time-sensitivity of the polonium-210 isotope and the volume of work involved in the cruise.

Table 2. Activities for filter aliquots processed by digestion or various leaching methods.**

Method	^{210}Po (dpm/100 m^3 air)
Digestion (10mL of HCl, HNO_3, HF, dry and dilute)	0.315 ± 0.013
Leaching (10mL of 6M HCl, 10mL of 8M HNO_3, dry and dilute)	0.329 ± 0.013
Leaching (20mL of 6M HCl dilute only)	0.250 ± 0.009
Leaching (10mL of 6M HCl, 10mL of 4M HNO_3, dilute only)*	n/a

*dissolved planchet

** Sample collection occurred from 5/22/2015 through 5/23/2015, and Po-210 plating was performed on 5/24/2015, after the leaching (1 hour total), digestion (12 hours), and drying (~6-8 hours) was performed for appropriate samples.

The ^{210}Pb, ^{210}Po, and ^{7}Be activities of ice-rafted sediments (IRS) from the Clinton River were also analyzed to prepare for chemical processing of Arctic IRS during the expedition. The main objective of this experiment was to gain familiarity with the protocol and techniques, but the experimental results have proven interesting enough to necessitate further study. Approximately 12L of ice was collected near the mouth of the Clinton River using a 20L plastic bucket. After melting (melt volume = 8.7L) , settling (48 hours), decanting, and drying the concentrated solution in an oven (48-72 hours), the total amount of silty-clay sediment collected was 3.6166g. The decanted ice solution was allowed to settle (48 hours) and then dried in the same manner, providing a total amount of clay sediment of 0.2418g. The sediments overall were fine-textured and grayish-brown, and included a small amount of organic material which was removed before leaching (grass, hairs). Sediment samples were leached with 6M HCl. The ^{210}Po/^{210}Pb activity ratios for the silty-clay, clay, and silty-clay leachate sediment sample were 0.43, 0.26, and 0.35, respectively (^{210}Pb = 434.4 ± 3.7, 704.9 ± 10.7, 526.1 ± 10.7 dpm/g, respectively; ^{210}Po = 184.9 ± 4.9 dpm/g) (Table 3). It is hypothesized that the high activity of lead-210 in the IRS sample is due to increased scavenging by re-suspended sediments. The mixing of sediments in the water column increases adsorption of atmospherically-deposited

isotopes from surface waters (beryllium-7 present in the sample is also atmospherically-deposited (Table 3)). The disequilibria of the ^{210}Po-^{210}Pb pair has not been widely studied in freshwater systems, and this is the first study showing that there is a large enrichment (more than by a factor of 100-300) compared to sedimentary material.

Table 3. ^{210}Pb, ^{210}Po, and ^{7}Be activities in Clinton river ice-rafted sediment samples.*

Sample	^{210}Pb Activity (dpm/g)	^{7}Be Activity (dpm/g)	^{210}Po Activity (dpm/g)	^{210}Po/^{210}Pb Activity Ratio
Clinton River sediment (silty-clay)	434.4 ± 3.7	228.6 ± 0.9	-	0.43 ± 0.08**
Clinton River sediment (clay)	704.9 ± 10.7	364.7 ± 4.2	-	0.26 ± 0.05**
Clinton River sediment (silty-clay leachate)	526.1 ± 8.3	246.7 ± 3.1	184.9 ± 4.9	0.35 ± 0.07

* Sample was collected from the mouth of the Clinton River on 3/16/2015 and plated for Po-210 on 4/16/2015. The activities were corrected for decay and in-growth.
**^{210}Po Activity for silty-clay leachate used to calculate the ratio.

2.5 Physical and biological parameters

Physical and biological parameters which are useful to correlate with radionuclide data analyses were also measured by various crew on the expedition. Salinity, temperature, and depth were measured using the ODF rosettes employed to collect water samples for radionuclide assay. The samples collected in ODF rosettes were also used to measure dissolved oxygen and inorganic nutrients including nitrate, nitrite, phosphate, and silicate for every bottle collected at each sampling station. This rosette was also used to collect samples for pigment analysis, which consisted of 2-L samples which were filtered and retained on glass fiber filters, stored in cryovials, frozen, and shipped to Oregon State University for analysis. Further details on the processing of ancillary parameters can be found in the US Arctic GEOTRACES Cruise Report (2015).

CHAPTER 3

RESULTS AND DISCUSSION

3.1 Ice-rafted sediments

3.1.1 Activities of ^{210}Po, ^{210}Pb, ^{226}Ra, and ^{210}Pb$_{xs}$ in ice-rafted sediments

The activities of total ^{210}Po and ^{210}Pb in IRS varied from 0.82 to 78 dpm/g (mean = 22 ± 1; n = 12) and 2.25 to 192 dpm/g (mean = 52 ± 2; n = 12), respectively (Appendix B). The German-collected samples will be referred to as "near-shelf" IRS (collected at 84°N and 116 to124°E) and US-collected samples will be referred to as "interior" IRS (collected at 87 to 88°N and 150 to 179°W) - a distinction which is highly relevant to the differences observed in the two datasets. The total ^{210}Po and ^{210}Pb activities of near-shelf IRS ranged from 0.82 to 4.24 dpm/g (mean = 2.3 ± 0.1; n = 6) and 2.25 to 4.93 dpm/g (mean = 3.37 ± 0.04; n = 6), respectively. In contrast, the ^{210}Po and ^{210}Pb activities of interior IRS were generally at least one order of magnitude greater, ranging from 7 to 78 dpm/g (mean = 42 ± 1; n = 6) and 21 to 192 dpm/g (mean = 100 ± 2; n = 6), respectively (Appendix B). The total ^{210}Pb activities can be compared to earlier published values of 8.60 to 159.0 dpm/g (Baskaran 2005). The total ^{210}Po/^{210}Pb activity ratios in near-shelf and interior IRS varied from 0.36 to 1.24 and 0.30 to 0.49, respectively (Appendix B).

The average measured ^{226}Ra for the interior and near-shelf IRS samples was 1.02 ± 0.25 and 1.82 ± 0.20 dpm g^{-1}, respectively, which is comparable to the values reported for benthic sediments in the coastal and shelf regions of the Arctic region (1 to 2 dpm/g; summarized in Baskaran 2005). Because ^{238}U is ubiquitous in the Earth's crust, its progeny, ^{226}Ra, is commonly found in sediments. Therefore, ^{210}Pb in IRS may be derived from ^{226}Ra which is intrinsic to the sediments, or from atmospherically-delivered ^{210}Pb. The latter source is referred to as ^{210}Pb$_{xs}$ (for

^{210}Pb "excess"), and is determined by subtracting the ^{226}Ra activity from the total measured ^{210}Pb activity based on the concept of secular equilibrium ($^{210}Pb_{xs} = {}^{210}Pb_{total} - {}^{226}Ra$) (Baskaran 2005). The $^{210}Pb_{xs}$ activities of interior IRS are 1 to 2 orders of magnitude higher than benthic sediments (ranging from approximately 20-192 dpm/g for the interior sediment samples, and from approximately 0.4 - 3 dpm/g for the near-shelf sediment samples) indicating that 1) the majority of total ^{210}Pb measured in interior IRS is derived by enrichment, and 2) greater enrichment occurred in interior IRS than near-shelf IRS (Appendix B). Enrichment factors (EF) are used to quantify the relative amount of enrichment of ^{210}Pb which has occurred, where EF = measured activity/benthic activity (Baskaran 2005). The EF values for this sample suite ranged from 1.2 - 188 (n=12; mean = 50), with the near-shelf sediments representing EF values closest to equilibrium, indicating far less enrichment than the interior IRS. This can be compared to the values of 4 to 92 (with $^{210}Pb_{xs}$ ranging from 7.4 to 175 dpm/g) reported by Baskaran (2005). The differences in specific activities, activity ratios, and enrichment factors can be attributed to the differences in the life history of IRS, their extent of interaction with seawater, and the time elapsed since the incorporation of ^{210}Pb into IRS, which are discussed further in sections 3.1.2 and 3.1.3.

3.1.2 'Age' of ice-rafted sediments

If the ^{210}Pb incorporation into IRS is a one-time event (such as incorporation to sediment during one melt-freeze cycle within a short period of time), and the IRS system remains closed, we can utilize the measured $^{210}Po/^{210}Pb$ AR to determine the 'age' (or residence time) of IRS (time since ^{210}Pb incorporation into the sea ice). The residence time is acquired through the following steps:

$$D = P_i - P \qquad \text{Eq (7)}$$

where D is the number of daughter atoms, P_i is the initial number of parent atoms, and P is the number of measured parent atoms. Using the principle of first-order radioactive decay, Eq (7) can be expressed as follows:

$$D = P_i - P_i e^{-\lambda t} \quad \text{Eq (8)}$$

This equation can be rearranged to solve for time according to Eq (9):

$$t = (-1/\lambda)\,[\ln\,(1 - D/P_i)] \quad \text{Eq (9)}$$

by substituting the D/P_i term with the change in activity ratios, the in-growth time (i.e. residence time) is calculated by the following equation:

$$t = (-1/\lambda)\,[\ln\,(1-((^{210}Po/^{210}Pb)_{xs} - (^{210}Po/^{210}Pb)_{initial})] \quad \text{Eq (10)}$$

where t is the in-growth period, and λ is the decay constant of ^{210}Po ($\lambda = (\ln(2))/t_{1/2}$). The following assumptions are made in order to use in-growth as a dating tool: i) there is no fractionation between ^{210}Po and ^{210}Pb during ice-rafting or when snow is compacted to form Arctic ice, and ii) the system remained closed since the initial incorporation of ^{210}Po and ^{210}Pb (there is no exchange of ^{210}Po and ^{210}Pb from water into or out of IRS). This implies that the incorporation of excess ^{210}Pb is a one-time event (or multiple events took place in a relatively short time-interval such as a week or so) during the melt season and subsequently it remained as a closed system. An initial activity ratio of 0.043 ± 0.004 was used based on the average ratio measured from fourteen aerosol deployments (^{210}Po/^{210}Pb AR range of aerosols = 0.003 to 0.097) (Appendix A). The calculated residence times are given in Table 4. The estimated residence times ranged from 56-136 days. The residence time of most of the near-shelf IRS samples are not datable because the total activities are closer to the parent-supported activity (i.e. benthic activity). Because of this, the total activity is too low to get a reliable excess activity (see $(^{210}Po/^{210}Pb)_{xs}$, Appendix B). The two datable near-shelf IRS samples gave an average residence

time of 102^{+30}_{-25} d (standard deviation = 48; n = 2). These residence times are therefore comparable to the interior IRS samples, which ranged from 56-117 days (mean = $83.8^{+5.0}_{-5.2}$ d; standard deviation = 22; n = 6). Based on an accepted average IRS residence time of 3 years, these values indicate that this sediment was sampled from first or second year ice (Nürnberg et al. 1994; Baskaran 2005). The variations in activity and high standard deviations for these samples reflect the large degree of heterogeneity in IRS. This is often observed in Arctic IRS and referred to as "patchiness", which is likely due to variations in the sediment origin, mechanisms of radionuclide incorporation and IRS transport.

In order for the calculated age by this in-growth method to be considered reliable, the ^{210}Po/^{210}Pb activity ratio in aerosols must be a valid representation of the initial input of these nuclides into IRS. There are a number of factors to consider when making this assumption. First, it is necessary to consider whether or not samples can be preferentially enriched due to grain size, with smaller size fractions (having greater surface area to volume ratios) adsorbing more ^{210}Pb than larger grain sizes. Cooper et al. (1998) reported the activities of ^{137}Cs and ^{239,240}Pu in IRS are independent of grain-size, suggesting that this factor does not contribute to radionuclide distribution in IRS. Second, the presence of biogenic material within IRS could increase the activity of ^{210}Po and ^{210}Pb in IRS due to its ability to adsorb both radionuclides, and its ability to assimilate and accumulate ^{210}Po. Therefore, a visual inspection of samples for biogenic material was conducted before processing the samples onboard. The most important factor which affects ^{210}Po and ^{210}Pb activity in IRS is the extent to which IRS has become enriched or depleted of radionuclides by surrounding water during melting/refreezing cycles. This includes enrichment by IRS entrapment in cryoconite holes through which meltwater flows. The transfer of ^{210}Pb from snow or sea ice onto IRS must involve water and hence during this process additional ^{210}Pb

may be picked up from the meltwater as well as surface waters. Therefore, the possible sources of $^{210}Pb_{xs}$ to IRS include: i) scavenging by IRS from the underlying water during direct contact over an extended period soon after entrainment or by exposure during reworking of ice; ii) direct atmospheric deposition onto sea ice followed by incorporation into sea ice-bound sediments during melting/refreezing cycles; and iii) particulate matter trapped in porous sea ice serving as a sieve, by picking up additional ^{210}Pb when surface water flows through the porous particle-laden sea ice. It was shown that if all $^{210}Pb_{xs}$ in IRS is derived from surface seawater, then each gram of the IRS is expected to be in contact with ~ $3m^3$ of water (Baskaran 2005). If IRS scavenges additional ^{210}Po and ^{210}Pb by any of the aforementioned sources after the initial incorporation of ^{210}Po and ^{210}Pb, then the calculated residence time of the sediments could be either an overestimate or underestimate depending on the $^{210}Po/^{210}Pb$ AR of the secondary radionuclide addition. In such a case, equation (10) is not suitable for age estimation. Further analyses are required to assess the degree of meltwater/surface water contribution to radionuclides in IRS. One useful parameter is the ^{7}Be activity measured in IRS. Because ^{7}Be is atmospherically-derived and short-lived ($t_{1/2}$ = 53.2d), ^{7}Be incorporation into IRS by meltwater or surface seawater is an indication that ^{7}Be incorporation took place recently (in weeks to ~3 months). Therefore, its presence in IRS indicates that at least a portion of the measured ^{210}Pb is derived from direct atmospheric deposition, and that its incorporation took place in less than 6 to 9 months. The presence of ^{7}Be was detected in the central Arctic (interior) IRS samples (with activities ranging from 0.15 to 11.9 dpm/g) (Appendix B). Similarly, the presence of ^{234}Th, an isotope found in seawater from the decay of dissolved ^{238}U rather than by atmospheric deposition, would indicate IRS interaction with seawater in less than ~ 2 months ($t_{1/2}$ = 24.1 d). There was no measurable ^{234}Th in this set of samples (Appendix B). Furthermore, the

distribution coefficient of ^{210}Pb is similar to that of plutonium, a radioactive isotope derived via nuclear fallout (International Atomic Energy Agency (IAEA) 1985). However, the latter isotope is no longer supplied by direct atmospheric deposition. Therefore, the samples can be analyzed for Pu to determine whether or not there is a strong enrichment of this isotope. If present, the IRS samples could potentially be enriched by surface or meltwaters in addition to aerosols. However, earlier studies did not show any significant enrichment of ^{239,240}Pu in IRS compared to benthic sediments (Baskaran 2005). Cesium-137, another radionuclide legacy of nuclear fallout, was not present in measurable quantities for any IRS samples in this study (Appendix B). It is nevertheless necessary to conduct future analyses and collaborations with participating principal investigators responsible for Pu data collection on the US GEOTRACES expedition in order to make this distinction.

3.1.3 IRS circulation and transport velocities

Ice circulation in the Arctic is predominantly controlled by the movement of the Beaufort Gyre and the transpolar drift stream (National Snow and Ice Data Center n.d.) (Figure 4). The Beaufort Gyre traps ice and recirculates it in a clockwise direction over relatively long spans of time, allowing it to become thicker and more deformed, prolonging its residence time to up to ten years (Rigor and Wallace 2004). In contrast, ice floes traveling within the transpolar drift stream (TDS) are often transported across the central Arctic and into the North Atlantic via the Fram Strait on a faster time scale (National Snow and Ice Data Center n.d.). The near-shelf IRS were collected from 84 31.40 N, 116 11.43 E (GERIRS 1) and 84 51.64 N, 124 11.69 E (GERIRS 2), which is approximately 737 km from the Siberian Shelf (Table 4, Figure 4). The interior IRS were collected closer to the North Pole, from 87 54.1 N, 179 43.429 W (E6195) and 88 58.393

N, 150 24.788 W (E6244), or approximately 1223 km from the Siberian Shelf. Therefore, the transport of sediments at both sample locations is predominantly controlled by the TDS.

Using the residence times and locations of the IRS in this study, it is possible to estimate their transport velocity (where the transport velocity = distance from the coastal site where IRS incorporation likely took place to the sampling site/residence time). Given that the majority of IRS is incorporated into sea ice along the Siberian shelf and the incorporation of ^{210}Po and ^{210}Pb also takes place shortly thereafter, the transport velocity was calculated between this assumed origin, based on the nearest proximal shelf along the direction of the transpolar drift stream, and each of the two sets of stations, resulting in transport velocities of 0.080 ± 0.003 m/s (shelf to near-shelf sediments) and 0.17 ± 0.01 m/s (shelf to interior sediments). The near-shelf transport velocities are consistent with values determined previously by Eicken et al. 1997 (reported ice velocity = 0.04 m/s; reported IRS transport = 0.05 m/s), but the observed transport velocity of interior sediments is above the range of average sea ice velocities from 1978 to 2003 reported by the NSIDC (0.05 to 0.10 m/s) (National Snow and Ice Data Center n.d.). The ice floe drift speed is highly variable in both the Beaufort Gyre and Transpolar Drift Stream, such that these rates cannot be qualitatively accepted based on currently published data. Drift speeds can vary and even change directions due to low-pressure systems and weather events (National Snow and Ice Data Center n.d.). The higher rates reported here may be due to the recent strengthening of the TDS and Beaufort Gyre due to changes in Arctic Oscillation. The Arctic Oscillation (AO) indexes atmospheric circulation over the Arctic Ocean. Changes in AO polarity (i.e. positive versus negative phases) indicate changes in atmospheric pressure, which result in weaker or stronger winds, in turn affecting ocean currents. Within the last decade, as much as 90% of the Arctic has seen increased drift speed (and corresponding decrease in multiyear ice coverage),

which is attributed to the polarity of the Arctic Oscillation (Kwok et al. 2013). Furthermore, the faster rate calculated for the interior sediments may be influenced by relatively stronger adjacent drift speeds from the Beaufort Gyre. Figure 5 illustrates sensor-based Arctic sea ice vectors in May of 2015. Based on their location within the TDS, it is inferred that the IRS migrated at a faster speed nearer to the shelf (where the figure illustrates vectors closer to 0.10 m/s), and these vectors are larger along the projected migration path of the interior sediments. An alternative explanation for this discrepancy between AR-based velocities and satellite-based velocities is that the residence times calculated for the interior sediments are lower estimates. This could result from the preferential loss of ^{210}Po with respect to ^{210}Pb in IRS to meltwaters, or the preferential addition of ^{210}Pb onto IRS compared to ^{210}Po from meltwaters. In this instance, the near-shelf sediments, which are most likely incorporated into first-year ice and thus not subjected to melting, may be accurate, as validated by previous data (e.g. Eicken et al. 2002) as well as the satellite data illustrated in Figure 5. In contrast, the interior sediments are likely incorporated into multi-year ice. Therefore, the radionuclide concentrations in these sediments are subject to variation by melt season processes, violating the closed-system assumptions of the model, thereby underestimating its residence time and overestimating its transport rate.

Table 4. Estimated residence times of ice-rafted sediments at all sampling stations.

Sample ID	Latitude	Longitude	Residence time (days)*
E6195	87 45.1 N	179 43.429 W	117^{+6}_{-6}
			$93.5^{+5.2}_{-5.0}$
			$84.9^{+4.6}_{-4.5}$
E6244	88 58.393 N	150 24.788 W	$55.7^{+3.9}_{-3.8}$
			$95.3^{+6.8}_{-6.6}$
			$56.1^{+4.4}_{-4.3}$
GERIRS 1	84 31.40 N	116 11.43 E	68.4^{+22}_{-20}
			136^{+37}_{-31}
			N/A
GERIRS 2	84 51.64 N	124 11.69 E	N/A
			N/A
			N/A

*Asymmetric error due to exponential decay of isotopes.

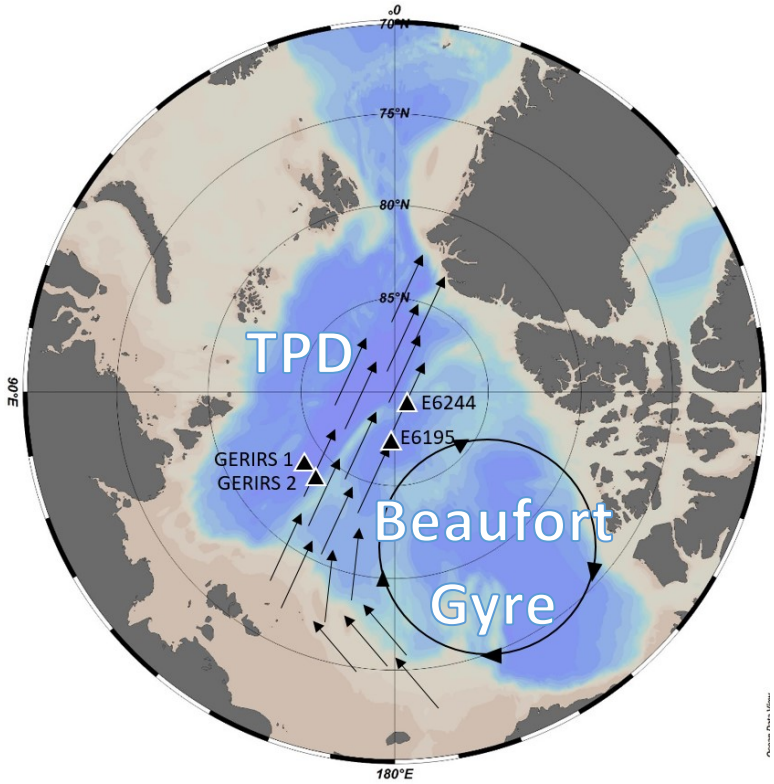

Figure 4. Major Arctic sea ice drift patterns.

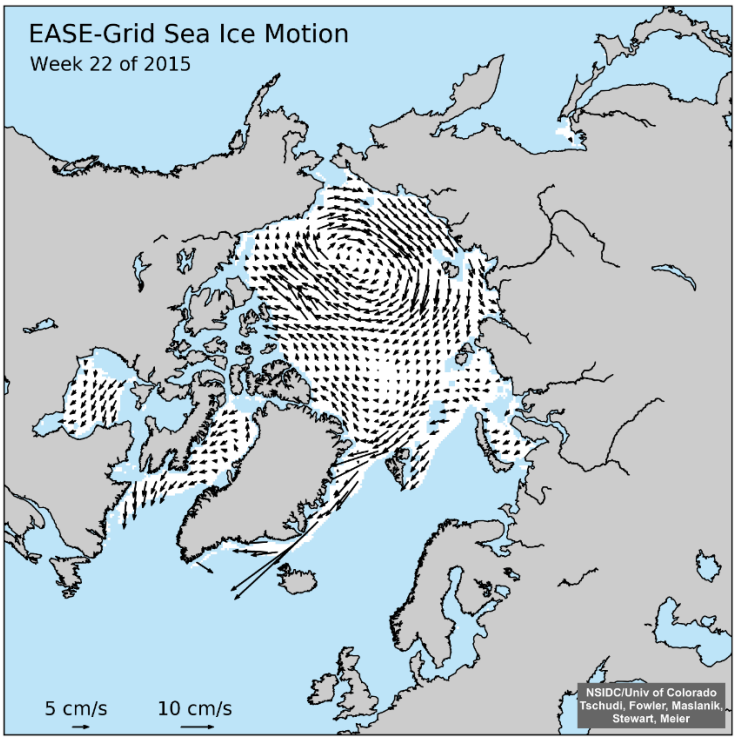

Figure 5. Sea ice velocity in Summer 2015 as determined from satellite data (National Snow and Ice Data Center n.d.).

3.2 ^{210}Po and ^{210}Pb studies in sea ice

3.2.1 Physical and biological characteristics of ice floes

The sea-ice minimum occurred on September 11, 2015, with the areal extent of ice dropping to 4.41 x 10^6 km^2 (compared to a sea-ice minimum of 6.12 x 10^6 km^2 in 1990; September sea ice extent decreased by approximately 13.3% per decade) (National Snow and Ice Data Center n.d.; "Arctic Sea Ice Minimum" n.d.). Sea-ice samples were collected from September 4-20, 2015, and thus samples collected reflect ice floe dynamics during the sea-ice minimum period. The thickness of ice floes sampled ranged from 120-180cm, with freeboard depths ranging from 2-28cm. Mean snow depth above ice cores ranged from 9-15cm. Melt ponds were sampled at all stations except ST-31, where no melt pond was accessible. Snow sample salinities were all 0 ppt (parts per thousand). Salinities increase with depth for all ice cores, from 0-3 ppt in general, with a maximum of 5.2 ppt measured in the middle sections of the ice core

from ST-43 (Figure 6). Surface ice salinities were an order of magnitude lower than bottom ice salinities (Figure 6, Table 5). Salinities measured in melt pond and under-ice seawater are compared to the salinities of the shallowest and deepest ice core segments in Table 5. Melt pond salinities were most variable, ranging from 0 – 30 ppt, and in most cases were higher than surface ice salinities (Table 5). Under-ice seawater was slightly lower than the generally-accepted salinity of seawater (35 ppt). This indicates the assimilation of melting bottom ice water into under-ice seawater during the melt season.

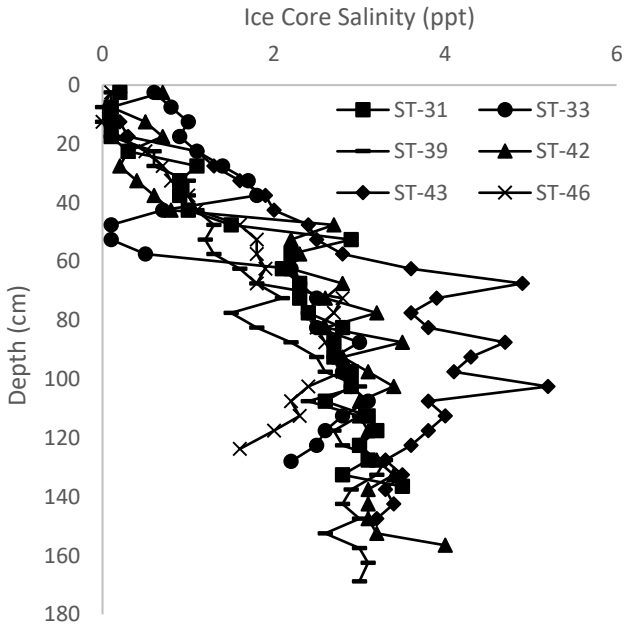

Figure 6. Salinity profiles of ice cores sampled at six ice stations.

Table 5. Salinity of melt pond, under-ice seawater, surface ice, and bottom ice.

	Salinity (ppt)			
Station	Melt Pond	Surface Ice	Under-Ice	Bottom Ice
31	n/a	0.2	30	3.5
33	0	0.6	30	2.2
39	11	0.1	35	3.0
42	2.5	0.7	30	4.0
43	30	0.2	30	1.0
46	2	0.1	30	1.6

3.2.2 Depositional fluxes of ^{210}Po and ^{210}Pb and activities in snow

The primary mechanism of ^{210}Po and ^{210}Pb removal from the atmosphere is by precipitation (both rainfall and snowfall) and dry deposition. The depositional flux of both ^{210}Po and ^{210}Pb can be determined by Eq (11)

$$depositional\ flux\ (dpm\ cm^{-2}y^{-1}) = activity\ in\ aerosol\ \left(\frac{dpm}{cm^2}\right) * deposition\ velocity\left(\frac{cm}{y}\right) \quad \text{Eq (11)}$$

where the specific activity of the nuclide in aerosols is multiplied by the assumed deposition velocity of aerosols, which is commonly assumed to be 1 cm s^{-1} (Turekian et al. 1977; Baskaran 2011). The blank-subtracted ^{210}Po and ^{210}Pb activities of aerosols ranged from 0.00039 to 0.12 dpm 100m^{-3} (mean = 0.031; n = 14), and from 0.056 to 2.15 dpm 100m^{-3} (mean = 0.73; n = 14), respectively (Appendix A). The lower activities observed in deployment 1 (^{210}Po = 0.0042 ± 0.0003 dpm 100m^{-3}; ^{210}Pb = 0.056 ±0.003 dpm 100m^{-3}) may be an artifact of sampling obstacles, where problems were reported by the technician. The depositional flux of ^{210}Po and ^{210}Pb ranged from 0.0003 to 0.0175 dpm cm^{-2} y^{-1} (mean = 0.0097; n = 14), and from 0.018 to 0.68 dpm cm^{-2} y^{-1} (mean = 0.23; n = 14), respectively (Appendix A). Depositional fluxes of ^{210}Po and ^{210}Pb across stations where snow and ice were sampled (deployments 5 through 10) ranged from 0.0003 to 0.0379 dpm cm^{-2} y^{-1} and 0.11 to 0.39 dpm cm^{-2} y^{-1}, respectively, with higher fluxes observed over ST-31 and ST-33, which correspond to the portion of the cruise transect closest to the Siberian Coast (Figure 2). This range of values agree with the compiled ^{210}Pb fallout flux values of 0.12±0.09 dpm cm^{-2}y^{-1}and 0.22±0.21 dpm cm^{-2}y^{-1} in the latitude belts of 60-70°N and 70-80°N, respectively (Baskaran, 2011). The flux of ^{210}Po is generally two or more orders of magnitude lower than ^{210}Pb flux, which is expected based on the very low ^{210}Po/^{210}Pb activity ratios of aerosols (AR range = 0.0090 to 0.097; mean = 0.043 ± 0.004; n = 14) (Appendix A).

The specific activities of ^{210}Po and ^{210}Pb in snow (stated as dpm 100L^{-1} of meltwater from snow) are reported in Appendix C. These activities were exceptionally high, ranging from 6 to 323 dpm 100L^{-1} (mean = 89 ± 6; n = 6) and from 192 to 1659 dpm 100L^{-1} (mean = 689 ± 11) for total (= dissolved + particulate) ^{210}Po and ^{210}Pb, respectively. The highest activities are observed at stations corresponding to the highest regions of ^{210}Pb depositional flux (ST-31 and ST-33) (Appendix A, Appendix C, Figure 1, Figure 2). However, the significance of this correlation is dependent on whether or not the rate of precipitation is the same in ST-31 and ST-33. On average, the dissolved fraction of snow samples accounted for 64% of ^{210}Po activity and 90% of ^{210}Pb activity, indicating the presence of ^{210}Po enrichment by particles. This is especially apparent in ST-31, which exhibited the highest total activities (^{210}Po = 323 ± 7 dpm 100L^{-1}; ^{210}Pb = 1659 ± 52 dpm 100L^{-1}), as well as the lowest relative dissolved ^{210}Po activity (32%), with ~68% of the total ^{210}Po associated with particulate matter. This is the first time, to our knowledge, that snow from the Central Arctic Ocean have been assayed for these nuclides, and thus, no published data are available for comparison. The ^{210}Po/^{210}Pb activity ratios in surface snow varied between 0.02 and 0.20 (n=6), with a mean value of 0.09 (Appendix C). This variation in activity ratio is likely due to variations in snowfall, as well as the time elapsed since the last snowfall. The residence time of snow can be calculated using Eq. (10), resulting in values ranging from 4 to 20 days (Appendix C). The observation that there is older snow indicates that the time required for snow to freeze into ice is relatively short (much less than the total duration of deposition during melt season). It is possible that the high magnitude of some activities found in snow is a result of i) the accumulation of nuclides in snow during precipitation events, or ii) the frequent deposition of nuclides on surface snow with a longer residence time.

3.2.3 Vertical variations of ^{210}Po and ^{210}Pb activities in ice cores

The total (= dissolved + particulate) ^{210}Po and ^{210}Pb activity in ice cores (stated as dpm 100L^{-1} of meltwater from segments of ice core) ranged from 1 – 141 dpm 100L^{-1} and 0.3 – 219 dpm 100L^{-1}, respectively (Figure 7, Appendix C). Activities in dissolved fractions were higher overall, with ^{210}Po and ^{210}Pb ranging from 1 - 96 and 0.3 - 174 dpm 100L^{-1}, respectively, versus particulate activities ranging from 0.2 - 75 and BDL – 120 dpm 100L^{-1}, respectively (Appendix C). The dissolved phase accounted for an average of 68% of total ^{210}Po activity and 79% of total ^{210}Pb activity. Particulate contribution to activity was greatest in the top segment (surface ice) (39% and 42% for ^{210}Po and ^{210}Pb, respectively). Activities in surface ice (approximately 0-30 cm in depth) were generally greater than deeper ice, which has also been reported by Masqué et al. (2007), who observed higher activities in the top 15.0-25.0 cm of two ice cores analyzed. The range of activities reported here are smaller than previously reported ranges (previously reported ^{210}Po = below detection limit to 540 dpm 100L^{-1}; ^{210}Pb = 60 to 1116 dpm 100L^{-1}) (Masqué et al. 2007). The total (= dissolved + particulate) ^{210}Po/^{210}Pb AR ranged from 0.1 to 5 (n = 31), and, with the omission of enriched segments (where ^{210}Po/^{210}Pb AR > 1), the range varied between 0.1 and 0.95 (n = 28) (Figure 8, Appendix C). The reason for the three ^{210}Po/^{210}Pb AR > 1 were from very low or BDL particulate ^{210}Pb (ST-31, ST-33), or from very low dissolved ^{210}Pb (ST-39).

3.2.4 Activities of ^{210}Po and ^{210}Pb in melt ponds and under-ice seawater

The activity of ^{210}Po and ^{210}Pb have never been measured in melt pond and under-ice seawater of the central Arctic and thus no data are available for comparison. Activities measured in melt pond water were highest at ST-43 and lowest at ST-31 with overall ^{210}Po and ^{210}Pb activities ranging from 11 to 61 dpm 100L^{-1} (mean = 28.1 ± 2.5 dpm 100L^{-1}; n = 5), and 25 to

204 dpm $100L^{-1}$ (mean = 93.6 ± 7.5 dpm $100L^{-1}$; n = 5), respectively (Appendix C). Activities measured in under-ice seawater were low compared to the aforementioned surface samples (snow, ice, melt pond), with average ^{210}Po and ^{210}Pb activities of 2.8 ± 0.3 and 9.2 ± 0.9 dpm $100L^{-1}$, respectively (n =6; ^{210}Po range = 0.7 to 10 dpm $100L^{-1}$; ^{210}Pb range = 4 to 20 dpm $100L^{-1}$; highest activities observed at ST-46; lowest activities observed at ST-33) (Appendix C). All surface samples were deficient in ^{210}Po with respect to ^{210}Pb (AR range: 0.02 – 0.52; n = 17). The $^{210}Po/^{210}Pb$ AR measured in snow samples were the lowest (0.02 – 0.20), and the AR in melt pond and under-ice seawater were similar (0.23 – 0.46 and 0.11 – 0.52, respectively). This ^{210}Po deficit is consistent with recently incorporated ^{210}Po and ^{210}Pb by atmospheric deposition, where the AR were all >0.10. These ratios correspond to a residence time of melt pond water of 47 to 61 days which is consistent with the fact that melt ponds occur during spring and summer months.

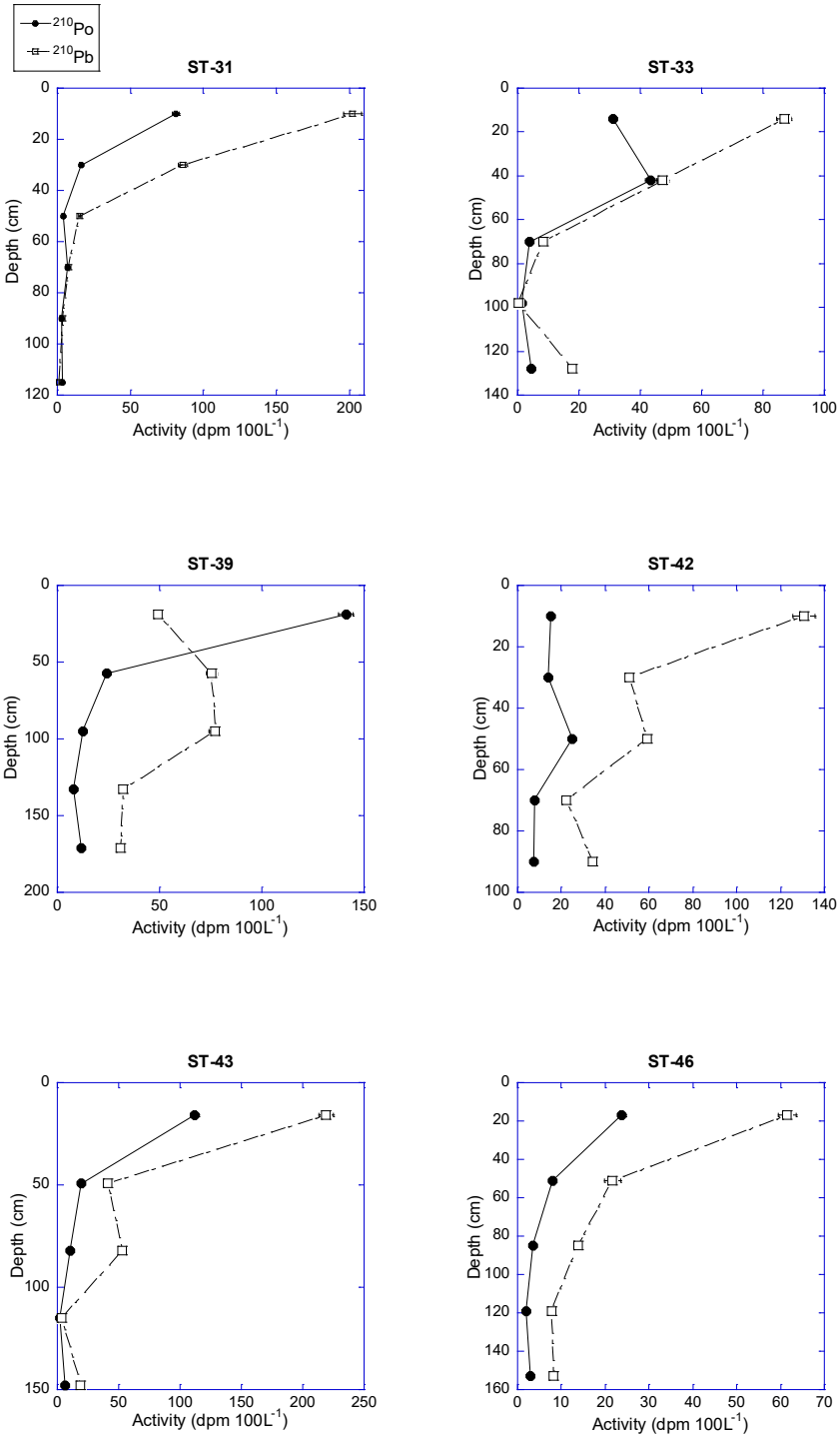

Figure 7. The total (= dissolved + particulate) ^{210}Po and ^{210}Pb activity profiles measured in ice cores at each station. Calculated error is included for all data points but not visible when marker is larger than the error bar. The error is the propagated error arising from counting statistics, error on the spike and chemical yield (in the case of ^{210}Pb).

3.2.5 Modeling ice floe accumulation and ablation rates

A large number of studies have been conducted on the mechanisms of ice accumulation and ablation. For this study, we propose three possible mechanisms for Arctic ice formation: Model (1) snow freeze; Model (2) seawater congelation; and Model (3) false bottom formation. Figure 10 illustrates each model as well as their predicted $^{210}Po/^{210}Pb$ AR trends. According to Model (1), ice sheets are formed by the accumulation of compacted snow, such that the oldest ice is at the bottom of the floe, and the newest ice is just below the snow layer. As ice grows, it is expected that the activity ratio value increases towards equilibrium (where $^{210}Po/^{210}Pb$ AR = 1) with time and thus depth. According to this model, the rate can be quantified using equation (12):

$$s = \Delta x/[(-1/\lambda)\ [\ln\ (1-((^{210}Po/^{210}Pb)_n - (^{210}Po/^{210}Pb)_{n-1})]] \quad \text{Eq (12)}$$

where n is the ice core segment, and at the ice – air interface n = 0. The denominator of this term (in-growth time) is derived in equations (7) through (9). By this model, accumulation rates are determined from the AR differences between segments. Ablation rates are determined from the differences in the activity ratios between the bottom layer of the ice floe and the underlying seawater based on the principle of hydrostatic equilibrium. However, it is likely that the activity ratio in water underneath the ice could be affected by preferential scavenging of ^{210}Po or ^{210}Pb. In fact, Arctic ice formation is too complex to use this simplified, closed-system model, which is immediately apparent upon review of the activity ratios for the six ice cores taken in this study (Figure 8).

Model (2) is based on the congelation of seawater to form ice. First year ice in the Arctic is generally formed first by the accumulation of frazil ice into either grease ice or pancake ice, depending on how calm or rough the surface ocean is (Figure 9) (National Snow and Ice Data Center n.d.). Ice then accumulates along the bottom of this thin sheet of ice by congelation

(Eicken et al. 1997). If an entire ice sheet was formed this way and was sampled, the $^{210}Po/^{210}Pb$ activity ratio would decrease with depth, as the youngest layer of ice would be newly formed at the bottom of the sheet (Figure 10). It is also possible for snow to accumulate, depress the freeboard of ice floes, mix with surface seawater, and freeze to form a top layer of ice. In this scenario, both Model 1 and Model 2 would be observed in the same ice core, and the oldest layer of ice would be located in the center of the floe (see Model (1) + (2); Figure 10).

Model (3) incorporates the potential effects of meltwater deformation on the structure of ice floes, which occurs in Arctic spring and summer (Figure 10). When atmospheric surface air temperatures are above freezing, ablation of surface ice floes occur, resulting in the formation of melt ponds (Alexandrov et al. 2013; Eicken et al. 2002) This melt pond water can percolate through the depth of the ice floe and form a lens of supercooled freshwater at the interface between the ice floe and surface seawater, which ultimately grows into a horizontal ice sheet known as false-bottom ice (Alexandrov et al. 2013; Untersteiner and Badgley 1958; Cherepanov et al. 1989; Eicken 1994; Eicken et al. 2002; Perovich et al. 2003; Polashenski et al. 2011). The previously reported extent of false bottom is from a few to several meters laterally and a few decimeters in depth (Alexandrov et al. 2013; Eicken et al. 2002). The corresponding AR trend would show equilibrium closer to the surface of the ice (assuming initial formation by seawater congelation) as well as with depth, from the refreezing of percolated surface meltwaters (Figure 10). There are multiple reasons why the ice cores sampled in this study could conceivably illustrate meltwater deformation and the presence of false bottoms. First, the cores were taken in the late Arctic summer, when false bottoms are commonly present. Second, the “rotted” texture of the ice cores is consistent with meltwater deformation. Third, the cores were all extracted within proximity of a melt pond (note that despite the absence of melt pond data from ST-31, a

melt pond was still present but frozen over and therefore samples could not be taken). Last, the ice floes sampled were characterized as second year ice floes, which are more prone to false bottom formations due to their greater permeability (Polashenski et al. 2016).

The use of Models (2), (1) + (2), and (3) does not allow the quantification of ice ablation because the bottom ice – under-ice seawater interface can no longer be characterized as a zone of ablation. Instead, it is more likely that bottom ice accumulation and false bottom formation is occurring at this interface. It is also possible that various combinations of these three models can be used to describe a single ice core. Indeed, accumulation rates were calculated in this study by assigning the most applicable model to every pair of segments (based on AR trend) for each ice core. Calculated accumulation rates range from 0.08 to 7 cm per day, with an average rate of 1.4 cm per day. Ice floe accumulation rates are previously reported to be as fast as a few centimeters per day (Alexandrov et al. 2013; Notz et al. 2003). Based on this data, congelation represents the major source of ice floe formation (Table 6).

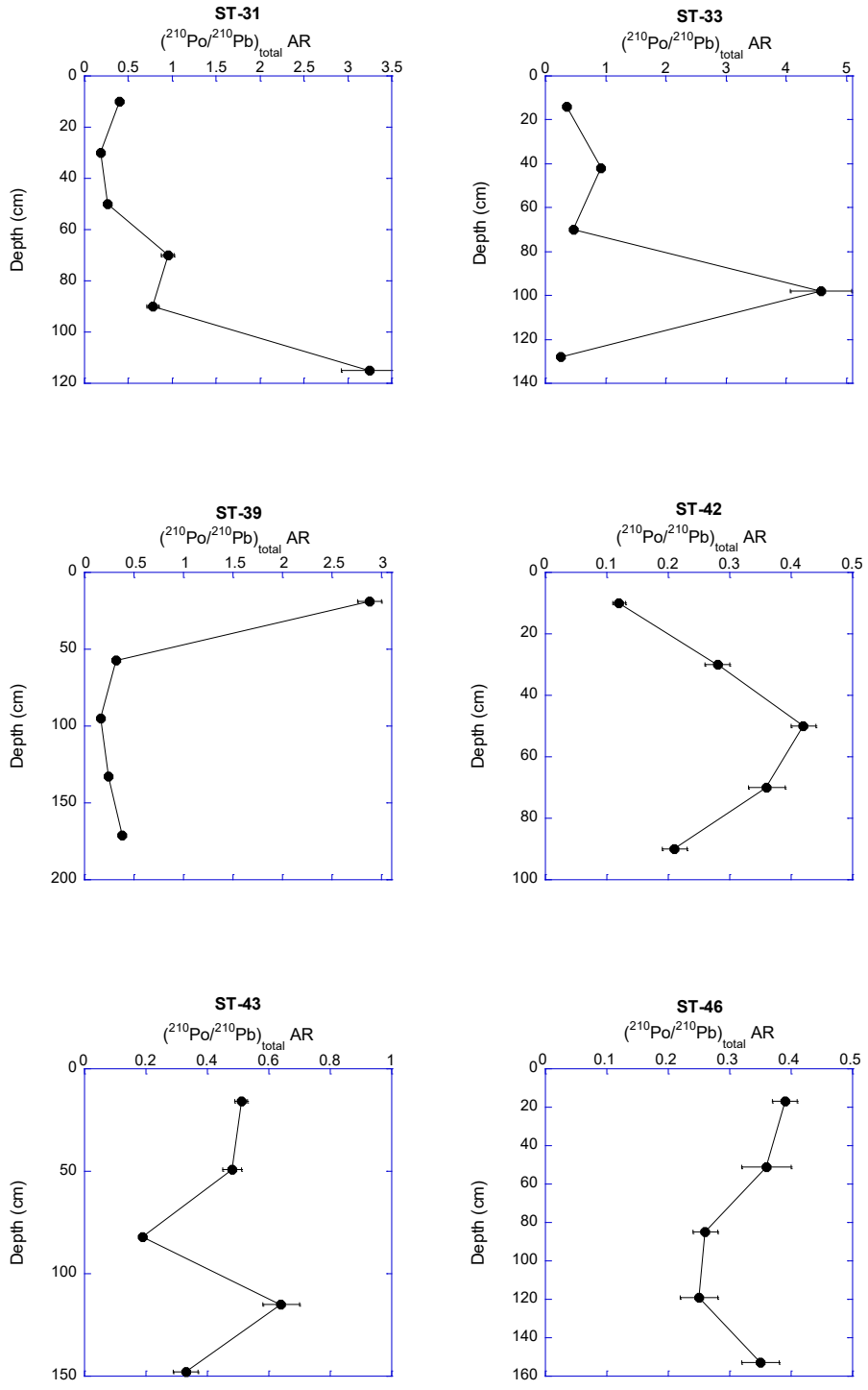

Figure 8. Activity ratio profiles with depth for each ice core.

Figure 9. An example of pancake ice in the marginal ice zone of the Arctic.

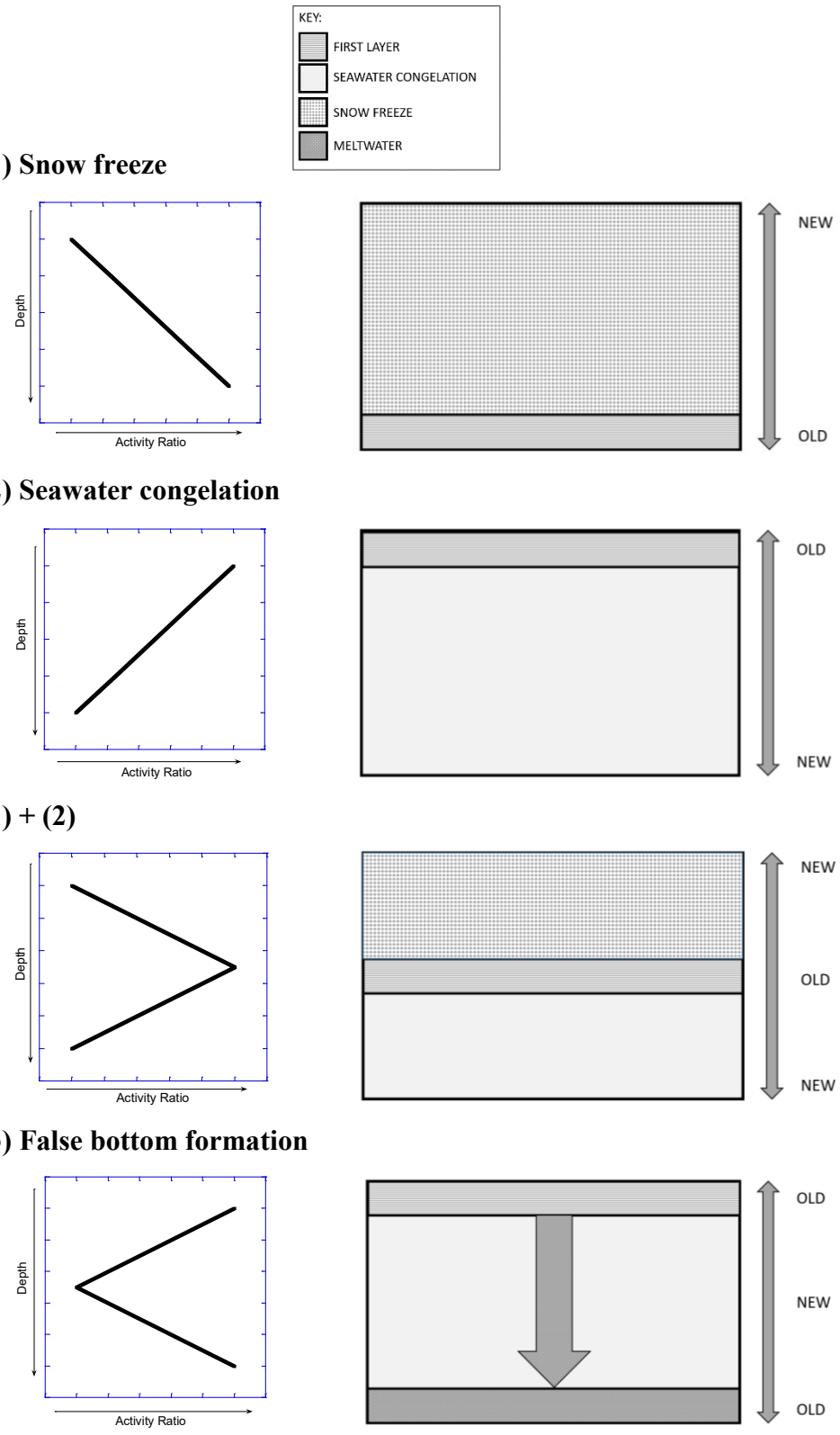

Figure 10. Proposed models of ice floe formation. The images on the right illustrate vertical cross-sections of ice floes with layers indicating the source of ice (first layer = pancake/frazil ice; seawater congelation = ice formed from seawater freezing and accumulating underneath first

layer; snow freeze = snow packed and frozen into ice; meltwater = water from melted ice which refreezes into ice). The graphs at left illustrate the proposed AR trend associated with the mechanism of ice formation.

Table 6. Accumulation rates calculated between each segment of each ice core sampled, and corresponding accumulation type used to model this rate.

Station	Depth Range (cm)	Accumulation Rate (cm/d)	error	Accumulation Type
31	10 - 30	0.43	0.03	Congelation
	30 - 50	1.46	0.13	Congelation
	50 - 70	0.08	0.01	False bottom
	70 - 90	0.55	0.07	Congelation
33	14 - 42	0.17	0.01	Snow freeze
	42 - 70	0.23	0.03	Congelation
39	57 - 95	1.12	0.08	Congelation
	95 - 133	2.32	0.21	False bottom
	133 - 171	1.34	0.12	False bottom
42	10 - 30	0.58	0.05	Snow freeze
	30 - 50	0.64	0.05	Snow freeze
	50 - 70	1.53	0.14	Congelation
	70 - 90	0.65	0.07	Congelation
43	16 - 49	4.98	0.35	Congelation
	49 - 82	0.49	0.04	Congelation
	82 - 115	0.28	0.03	False bottom
	115 - 148	0.44	0.06	Congelation
46	17 - 51	7.68	0.84	Congelation
	51 - 85	1.52	0.20	Congelation
	119 - 153	1.63	0.24	False bottom

3.2.6 Open System Considerations

It is clear that the vertical distribution of ^{210}Po and ^{210}Pb in Arctic ice floes is complicated and requires further study. The rates presented in Table 6 must be considered preliminary until additional parameters are available for analysis. These include stable isotope oxygen data to assess the source of ice (whether meteoric in origin (i.e. snow) or from surface seawater), and pigment distribution in ice cores, which will show if biogenic particle enrichment of ^{210}Po is present. The main assumption of the false bottom model (Model (3)) that must be validated is that the ^{210}Po/^{210}Pb activity ratios of percolated and refrozen meltwater are conservative. If ^{210}Po

or ^{210}Pb are exchanged between percolating meltwater, ice, and under-ice seawater (i.e. if activity ratios are non-conservative during melt season deformation), then the AR values measured in each ice core segment cannot be used in rate quantification. Therefore, interaction between meltwater and the ice through which it percolates must be better understood. This data illustrates that the salinity of percolating meltwater is likely not conservative. According to Untersteiner (1968), percolating meltwater decreases the salinity of ice as it permeates through the ice floe. This may be responsible for the higher salinity observed with depth for each ice core (Figure 6). Alternatively, the bottom ice may be incorporating surface seawater and its associated brine through cavities present in the ice, indicating the transport of water and possibly radionuclides across this interface. Moreover, if most Arctic sea ice forms by the congelation of seawater, then the surface ice layer is possibly exposed to prolonged ^{210}Pb deposition relative to the newly formed bottom layers. This introduces another problem that the accumulation rate calculation does not account for. Further questions that must be answered include 1) how do meltwater ^{210}Po/^{210}Pb activity ratios translate to false bottoms (are the activity ratios the same in meltwater and false bottom); 2) what percentage of meltwater percolates and/or becomes a false bottom, and 3) what other scenarios may affect the mobility of ^{210}Po and ^{210}Pb across the meltwater-ice and ice-seawater interfaces. Finally, it is essential to determine whether the vertical ^{210}Po/^{210}Pb AR patterns observed here simply reflect the open system exchange of radionuclides across all interfaces, making this, or any isotopic dating technique, unreliable. Based on these uncertainties, future research is necessary in order to confirm or correct the ^{210}Po/^{210}Pb activity ratio approach to ice floe accumulation rate quantification, which has been proposed here for the first time.

3.3 Vertical seawater profiles

3.3.1 Physical and biological characteristics of water column

Temperature profiles indicate that the mixed layer extended to approximately 100m at ST-30 and ST-43, however, the mixed layer is less clear for ST-30, with a spike of warmer water observed ~50 m (Figure 11). The thermocline was located at ~500m for both stations, and the halocline was observed ~200m (Figure 11, 12). Inorganic nutrients (SO_4, NO_3, NO_2, PO_4) measured in the mixed layer were slightly lower than measured values in 2012 and could suggest a recent export event (Fernandez-Mendez et al. 2015). Such differences could also be due to the spatial and temporal differences between these two data sets. At ST-30 silicate concentration reached a maximum of 16.6 µmol kg-1 at 73m, and at ST-43 silicate concentration reached a maximum of 34.7 µmol kg-1 at 100m (Figure 13). Minimum silicate concentrations were 5.28 (at 126m) and 6.05 (at 330m) µmol kg^{-1} at ST-30 and ST-43, respectively. Silicate concentration was the highest compared to other inorganic nutrients in the mixed layer (Figure 13). The measured N:P and N:Si ratios were 4 and 0.3, respectively, which are both at the low end of the ranges reported for the central Arctic during the 2012 sea-ice minimum (3-9 and 0.3-1.7, respectively) (Fernandez-Mendez et al. 2015).

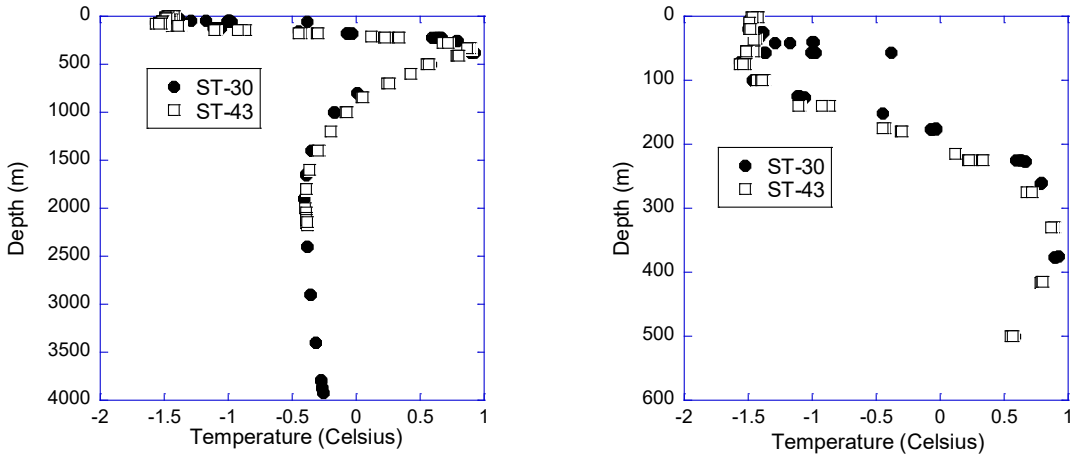

Figure 11. Temperature profiles measured at ST-30 and ST-43 (upper 500m profile indicates mixed layer depth of ~100m).

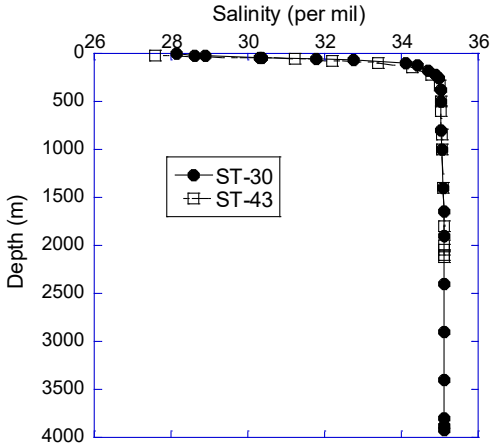

Figure 12. Salinity profile measured at ST-30 and -43.

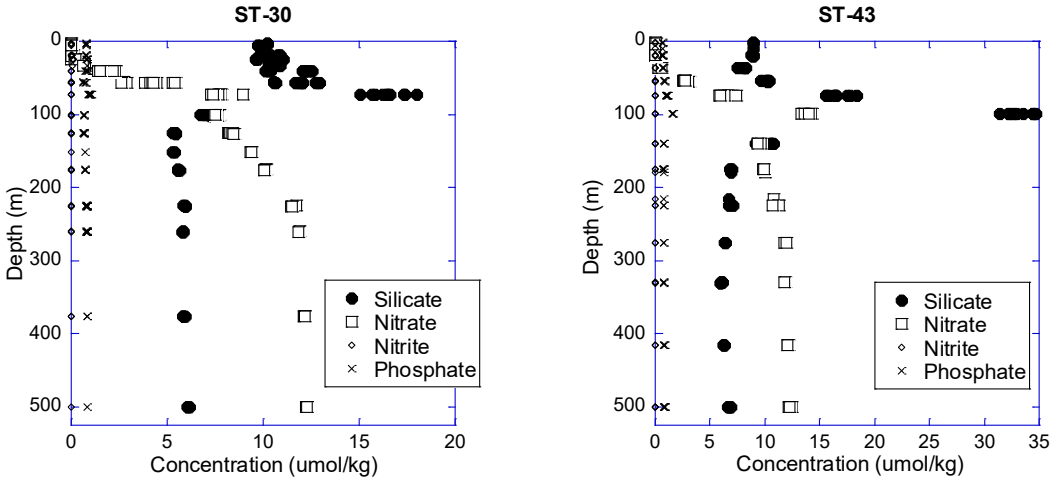

Figure 13. Inorganic nutrient profiles in upper 500m of ST-30 and ST-43.

3.3.2 Activities and activity ratios of ^{210}Po and ^{210}Pb in seawater

3.3.2.1 Activities of ^{210}Po and ^{210}Pb in the water column

The total (= dissolved + particulate) activities of ^{210}Po and ^{210}Pb measured at ST-30 and ST-43 ranged from 0.46 to 16.6 dpm 100L^{-1} and 1.18 to 32.5 dpm 100L^{-1}, respectively (Figure 14; Appendix D). In general, the specific activities in the dissolved phase were greater than in the particulate phase, with dissolved activities accounting for ≳ 50% of total activities (Figure 14). The dissolved ^{210}Po and ^{210}Pb activities in both stations ranged from 0.29 to 15.3 dpm 100L^{-1} and 0.18 to 30.2 dpm 100L^{-1}, respectively. Total particulate (= >51 μm + 1-51 μm) ^{210}Po and ^{210}Pb activities ranged from 0.04 to 7.55 dpm 100L^{-1} and 0.66 to 6.31 dpm 100L^{-1}, respectively. Small particulate fractions were generally higher in activity than the large particulate fractions, with <51μm particle size fractions accounting for ~92% of the total particulate ^{210}Po activity and ~83% of the total particulate ^{210}Pb activity (mean ^{210}Po and ^{210}Pb activities in > 51 μm particulate samples: 0.22 and 0.34 dpm 100L^{-1}, respectively; mean ^{210}Po and ^{210}Pb activities in 1-51 μm particulate samples: 1.33 and 1.88 dpm 100L^{-1}, respectively). Surface (upper 100m) total

^{210}Po and ^{210}Pb activities at both stations range from 0.57 to 5.69 and 1.18 to 10.97 dpm 100L^{-1}, respectively (Figure 18, Appendix D). Maximum total ^{210}Po and ^{210}Pb surface activities at both ST-30 and ST-43 are observed at 20 to 24 m (Figure 18). Lower activities of ^{210}Pb were observed in the halocline, which has been consistently reported for Arctic profiles and is attributed to the transport of depleted shelf waters by mixing or advection (Smith et al. 2003). There is an overall general increase with depth in the activities of particulate and dissolved (as well as total) activities of both ^{210}Po and ^{210}Pb in both stations (Figure 14, Appendix D).

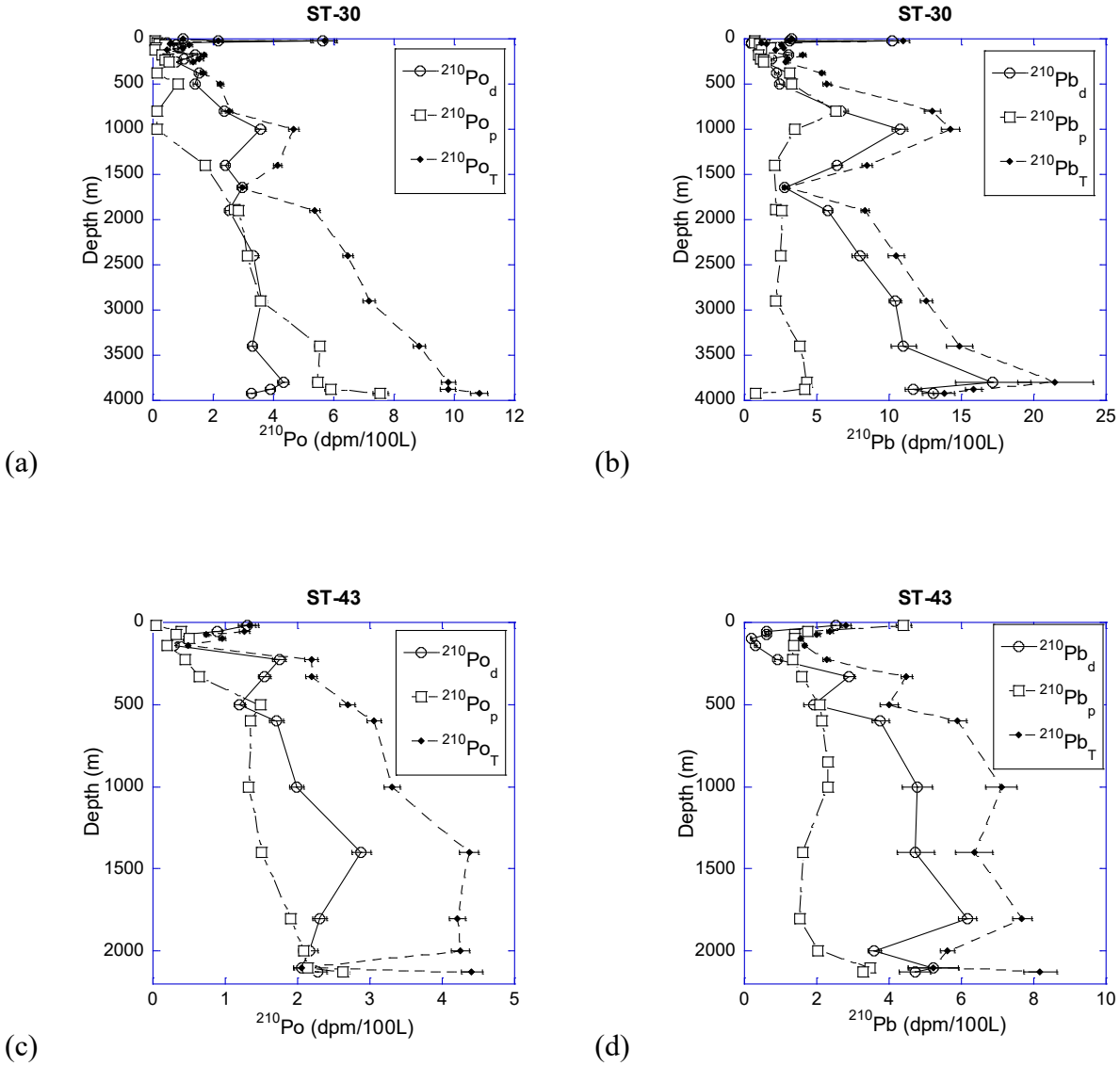

Figure 14. Dissolved, particulate, and total ^{210}Po activity profiles for (a) ST-30 and (c) ST-43, and dissolved, particulate, and total ^{210}Pb activity profiles for (b) ST-30 and (d) ST-43 (outlier removed in figure (d): 850 m; $^{210}Pb_d$ = 30.2 ± 1.2 dpm/100L and $^{210}Pb_T$ = 32.5 ± 1.2 dpm/100L).

3.3.2.2 ^{210}Po/^{210}Pb activity ratios in the water column

A significant ^{210}Po deficiency was observed throughout most of the water (39 out of 40 samples, and in one sample, the ^{210}Po/^{210}Pb AR = 1.06 in the dissolved phase and particulate samples were not available; Figure 15, Appendix D). In most major ocean basins in non-polar regions, the ^{210}Po/^{210}Pb activity ratio in the particulate phase [$(^{210}Po/^{210}Pb)_p$] was found to be

>1.0. In these non-polar regions, when particulate matter with $(^{210}Po/^{210}Pb)_p$ >1.0 undergoes sinking, a major fraction undergoes remineralization, thereby altering the $^{210}Po/^{210}Pb$ activity ratios in the deeper water column (Niedermiller and Baskaran, in revision). However, in both ST-30 and ST-43, above 1500 m, the $(^{210}Po/^{210}Pb)_p$ AR is <1.0. This observation is in contrast with the common observations in non-polar regions. The activity ratios based on the full inventories at each station were 0.51± 0.07 and 0.56 ± 0.07 for ST-30 and ST-43, respectively (Table 7, Table 8). Such disequilibria between total ^{210}Po and total ^{210}Pb have been reported at similar coordinates in the Arctic as well as other regions in the deep Arctic basins in previous studies: the Arctic Ocean Section (AOS) of 1994 sampled ^{210}Po and ^{210}Pb at nearby coordinates, with resulting inventory-based AR's ranging from 0.43 – 0.66 (Table 8; Smith et al. 2003; Tucker et al. 1996). More recently, samples collected in 2012, during the most recent sea-ice minimum on record, indicate ^{210}Po depletion in the upper water column (up to 100 m), with AR's as low as 0.21 ± 0.12 (Roca-Marti et al. 2016). The authors attributed such a deficit to early summer export. Indeed, due to the large disequilibria reported here, it is suggested that a scavenging event must have taken place more than a month before sampling, thereby assigning the export event to the early summer months of May-July. In contrast to these deficits are the higher activity ratios reported by Moore and Smith (1986) along the Alpha Ridge (inventory AR = 0.79 ± 0.04) (Table 8). Despite the location of both the CESAR station and ST-43 along the Alpha Ridge, these stations exhibited different radionuclide ratios. Such difference is likely due to differences in temporal ice coverage. The CESAR station is a permanently ice-covered station, with very low suspended particle concentration (~ 5 μg/L, Bacon et al. 1989). The depth-normalized inventory of particulate matter (≥0.45 μm) is about an order of magnitude lower in the CESAR station compared to deep basins in the Arctic Ocean (summarized in Trimble et al.

2004). Furthermore, the two stations were sampled during different seasons and therefore subject to differences in biological productivity (CESAR station was sampling in April-May of 1983; ST-43 was sampled in mid-September). It is also possible that the long-term changes in net primary productivity (NPP) could partially account for such differences, as NPP has seen an increase of at least 30% since 1998 (Arrigo and van Dijken 2015; Roca-Marti et al. 2016).

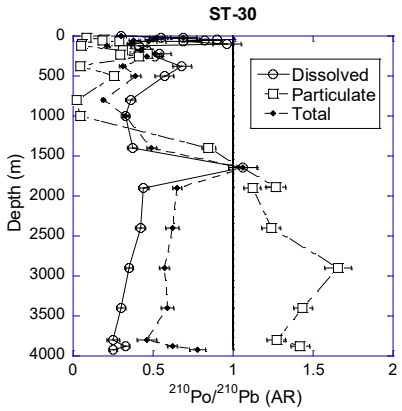

(a)

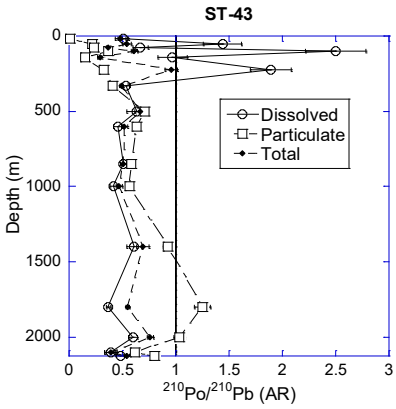

(b)

Figure 15. ^{210}Po/^{210}Pb activity ratio profiles (vertical line at x=1 represents equilibrium between parent and daughter isotope) for ST-30 and ST-43. One outlier removed from ST-30 plot to improve resolution of activity ratio scale (depth = 3925 m; $(^{210}Po/^{210}Pb)_p$ = 10.3).

3.3.2.3 ^{210}Pb/^{226}Ra activity ratios in the water column

The average ^{210}Pb/^{226}Ra activity ratios for ST-30 and ST-43 were 0.67 and 0.65, respectively, and thus closer to equilibrium than the ^{210}Po/^{210}Pb pair, with most ^{210}Pb depletion present in the upper 500 m (Figure 16). The total ^{210}Pb/^{226}Ra activity ratio in the upper 100 m at both stations varied between 0.12 and 0.98 (mean = 0.29), with no excess ^{210}Pb in the surface waters. Due to low depositional flux in the Arctic, annual ^{210}Pb production from ^{226}Ra appears to be higher than that from the atmospheric depositional flux. This is in contrast with all other non-polar ocean basins where the atmospheric depositional flux is the major dominant source of ^{210}Pb in the upper 100 m. In two samples (at depths 800 and 1000 m) at ST-30, the ^{210}Pb/^{226}Ra AR is

>1.0. This is attributed to lateral advection of particulate ^{210}Pb from the shelf region. A similar advectional source from the shelf region into the deep basin has been reported in earlier studies (e.g. Smith et al. 2003).

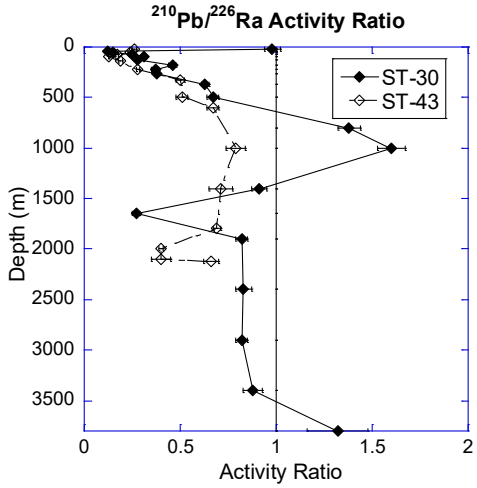

Figure 16. ^{210}Pb/^{226}Ra activity ratio profiles (vertical line at x=1 represents equilibrium between parent and daughter isotope) for ST-30 and ST-43. One outlier removed from ST-43 plot to improve resolution of activity ratio scale (depth = 850 m; activity ratio = 3.8). The ^{226}Ra data is not given in Appendix D, and is used with permission from Matthew Charette (WHOI).

3.3.3 Partitioning of ^{210}Po and ^{210}Pb: Fractionation factor

Since the gross disequilibrium between ^{210}Po and ^{210}Pb is prevalent throughout the water column, both in this study as well in other published studies in the Arctic, the preferential removal of ^{210}Po or ^{210}Pb needs further investigation. In order to further interpret ^{210}Po and ^{210}Pb scavenging by particles, the fractionation factor can be used to evaluate if there is any preferential scavenging of ^{210}Po and ^{210}Pb. The distribution coefficient of ^{210}Po and ^{210}Pb are determined as follows:

$$K_d^{Po} = \frac{A_{part-Po}}{A_{diss-Po}} * SPM \qquad \text{Eq (13)}$$

$$K_d^{Pb} = \frac{A_{part-Pb}}{A_{diss-Pb}} * SPM \qquad \text{Eq (14)}$$

Combining equations (13) and (14), the fractionation factor is determined as follows:

$$FF_{Po/Pb} = \frac{K_d^{Po}}{K_d^{Pb}} \qquad \text{Eq (15)}$$

A fractionation factor greater than one is indicative of the preferential scavenging of ^{210}Po over ^{210}Pb onto particulates. The fractionation factor for both ST-30 and ST-43 increased with depth (Figure 17). At ST-30, $FF_{Po/Pb}$ is less than one at 24 – 1000 m and greater than one at 1400 – 4000 m, indicating preferential scavenging of ^{210}Po by sinking particles. Likewise, at ST-43, $FF_{Po/Pb}$ less than one at 20 – 330 m and greater than one at 500 – 2200 m. One explanation for this observed trend is the release of exopolyomeric substances (EPS) in deeper waters from the sinking particulate matter. Sinking particles could release these compounds which would preferentially remove ^{210}Po over ^{210}Pb (Yang et al. 2013).

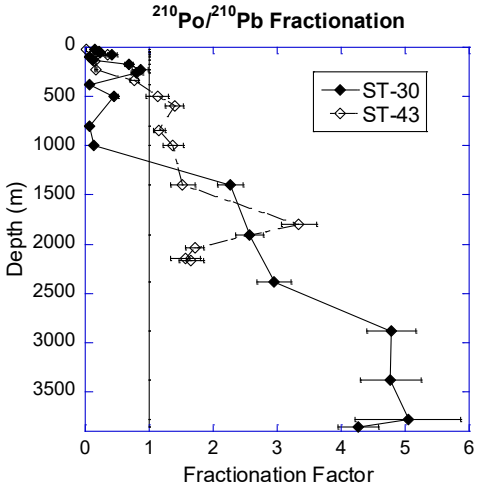

Figure 17. The ^{210}Po/^{210}Pb fractionation factors with depth at ST-30 and ST-43 (outlier excluded at 4000 m, where $FF_{Po/Pb} = 41 \pm 4$).

3.3.4 Residence times of ^{210}Po and ^{210}Pb in seawater

The residence time of ^{210}Po and ^{210}Pb can also be determined based on the following equation:

$$\tau = 1/\lambda_D * \frac{\frac{A_D}{A_P}}{1-\left(\frac{A_D}{A_P}\right)} \qquad \text{Eq (16)}$$

where D and P denote daughter and parent isotopes, respectively, and A is the inventory of the radionuclide for the whole water column. The ^{210}Po residence times at ST-30 and ST-43 were found to be $0.57^{+0.15/-0.09}$ y, and $0.68^{+0.10/-0.07}$ y, respectively (Table 8). The residence times obtained in this study can be compared to the values obtained from published data in the Arctic. For example, similar ^{210}Po residence times were calculated from the AOS 1994 cruise data (^{210}Po residence times are 0.42 – 0.49 y for stations 18 and 26 (Makarov Basin) while a longer residence time of 1.06 ± 0.17 y was obtained at station 35 (North Pole) (Table 8)). The longest calculated ^{210}Po residence time was observed at the CESAR station (2.05 ± 0.23 y; coastal Alpha Ridge) (Table 8). The suspended particle concentration in CESAR station is the lowest and hence the scavenging is poor. The suspended particle concentration and inventory is about an order of lower compared to deep water stations in the Arctic Ocean where there is seasonal ice cover. Lower SPM concentration is anticipated to result lower remineralization rate of sinking particulate matter and hence the ^{210}Po/^{210}Pb AR is expected to be higher. Thus, there is a coupling between the SPM inventory, residence time of ^{210}Po and remineralization of sinking particulate matter. In contrast to these ^{210}Po residence times, ^{230}Th residence times from previous studies show a longer residence time in the Makarov Basin than along the Alpha Ridge (45 versus 39 years) (Trimble et al. 2004).

The residence time of ^{210}Pb in the two stations were calculated to be 399^{+80}_{-72} y (ST-30) and 171^{+34}_{-20} y (ST-43) (Table 8). The ^{210}Pb residence time at the Makarov Basin station is

approximately two times the residence time at the Alpha Ridge station, which is similar to the residence time of ^{230}Th for the whole water column, with higher residence time of ^{230}Th in the Makarov Basin compared to Alpha Ridge station. Differences in residence times are generally due to differences in particle fluxes or ventilation timescales (Trimble et al. 2004). It is proposed here that both factors likely influence the residence times of this suite of radionuclides, and the contrasting timescales are a reflection of the differences in nuclide particle affinity. First, ^{210}Pb residence times are expected to be lower at the CESAR station than the interior stations due to boundary scavenging of particle-reactive radionuclides. Second, ^{210}Po residence times are more affected by biological activity, which would explain longer ^{210}Po residence time (assuming no significant remineralization of particulate ^{210}Po) observed at the CESAR station during the early spring (a time of lower productivity). Both ^{230}Th and ^{210}Pb are less affected by biological productivity than ^{210}Po, accounting for their longer residence times in Makarov Basin relative to ^{210}Po. The longer timescales of ^{230}Th and ^{210}Pb in the Makarov Basin relative to the Alpha Ridge are potentially due to the slower ventilation of the deep basin where the Lomonosov Ridge separates the Eurasian and Amerasian Basins.

Table 7. ^{210}Po, ^{210}Pb, and ^{226}Ra inventories: reported for this study and for other sources where stations had similar geographic coordinates (latter values are calculated based on reported activities).

ST #	Lat.	Long.	Depth	Inventory (dpm/m^2)*		
			(m)	^{210}Po	^{210}Pb	^{226}Ra**
30[1]	87N	179W	3925	212472 ± 3%	415788 ± 13%	449321 ± 12%
43[1]	85N	149W	2166	96358 ± 5%	173429 ± 11%	206063 ± 13%
18[2]	80N	173W	1500	12284 ± 11%	28241 ± 9%	n/a
26[2]	84N	175E	2000	26433 ± 10%	55683 ± 9%	n/a
35[2]	90N	180W	4210	81230 ± 18%	123065 ± 13%	n/a
CESAR[3]	85N	108W	1770	3957 ± 4%	5012 ± 4%	12523 ± 17%

[1]this study; [2]Smith et al. (2003); Tucker et al. (1996); [3]Moore and Smith (1986)
*errors given as percentages due to large values

**^{226}Ra inventories calculated based on data from Matthew Charette (WHOI); errors on activity estimated at 5%

Table 8. Full inventory-based activity ratios, export fluxes and residence times (RT): reported for this study and for other sources where stations had similar geographic coordinates (latter values are calculated based on reported activities).**

ST #	Depth (m)	^{210}Po/^{210}Pb (Inv. AR)	^{210}Po Export Flux (dpm m^{-2} d^{-1})	^{210}Po RT* (y)	^{210}Pb/^{226}Ra (Inv. AR)	^{210}Pb Export Flux (dpm m^{-2} d^{-1})	^{210}Pb RT* (y)
30[1]	3925	0.51 ± 0.07	1018 ± 142	$0.57^{+0.15}_{-0.09}$	0.93 ± 0.17	2.85 ± 0.52	399^{+80}_{-72}
43[1]	2166	0.56 ± 0.07	386 ± 46	$0.68^{+0.10}_{-0.07}$	0.84 ± 0.14	2.78 ± 0.47	171^{+34}_{-20}
18[2]	1500	0.43 ± 0.06	80 ± 11	0.42± 0.10	n/a	n/a	n/a
26[2]	2000	0.47± 0.06	146 ± 20	0.49± 0.07	n/a	n/a	n/a
35[2]	4210	0.66± 0.14	209 ± 29	1.06 ± 0.17	n/a	n/a	n/a
CESAR[3]	1770	0.79 ± 0.04	5.3 ± 0.3	2.05 ± 0.23	0.40 ± 0.07	0.64 ± 0.11	21 ± 2

[1]this study; [2]Smith et al. (2003); Tucker et al. (1996); [3]Moore and Smith (1986)
*asymmetric error due to exponential decay of isotopes – value calculated using upper and lower bounds of error.
**^{210}Pb/^{226}Ra AR, ^{210}Pb export flux, and ^{210}Pb RT calculated based on ^{226}Ra data used with permission from Matthew Charette (WHOI).

3.3.5 Export fluxes of ^{210}Po and particulate organic carbon (POC)

The disequilibrium between the ^{210}Po-^{210}Pb pair and ^{210}Pb-^{226}Ra pair can be used to determine the vertical export flux of the daughter isotope by use of a steady state box model. This model neglects lateral transport, advection, and diffusion into or out of a box. It is therefore based on the vertical transport of particle-reactive isotopes via sinking particles, and is modeled by the following equation (Buesseler et al. 1992; Roca-Marti et al. 2016):

$$F_D = \lambda_D(A_P - A_D) \qquad \text{Eq (17)}$$

where F_D is the export flux of the daughter isotope, and A_P and A_D are the inventories of the parent and daughter isotope (i.e. activities integrated with depth in the mixed layer or upper 100m), respectively. The ^{210}Po and ^{210}Pb export fluxes for the upper 100 m of ST-30 and ST-43 are given in Table 9. Reported ^{210}Po export fluxes in the world ocean range from 5 to >100 dpm m^{-2} d^{-1} (Roca-marti et al. 2016). Therefore, surface (<100m) ^{210}Po export fluxes reported here are

very low, ranging from 2.4 – 8.5 dpm m^{-2} d^{-1} , a reflection of the overall lower productivity in the Arctic Ocean relative to the world ocean (Table 9).

Table 9. Export fluxes of ^{210}Po and ^{210}Pb (dpm m^{-2} d^{-1}) at integrated depths (integrated from surface (depth = 0 m) to depth given).

		Export Flux (dpm m^{-2} d^{-1})	
ST #	Depth (m)	^{210}Po	^{210}Pb
30	25	2.4 ± 0.6	0.15 ± 0.03
	50	5.4 ± 0.8	0.33 ± 0.11
	100	8.5 ± 0.9	0.60 ± 0.31
43	25	1.5 ± 0.2	0.14 ± 0.01
	50	3.7 ± 0.6	0.37 ± 0.13
	100	6.1 ± 0.3	0.73 ± 0.21

Integrated ^{210}Po and ^{210}Pb activity in the surface waters (mixed layer up to 100m) can be used to determine the POC export flux in the vertical water column by the following equation:

$$POC\ Export\ Flux = F_D * \frac{POC}{A_D^{part}} \qquad \text{Eq (18)}$$

where F_D is ^{210}Po export flux (determined via ^{210}Po and ^{210}Pb inventory using Eq (17)), and $\frac{POC}{A_D^{part}}$ is the ratio of the particulate organic carbon (POC) concentration to the particulate ^{210}Po activity (in sinking particulate matter). While the analysis of POC data is still pending from this expedition, published POC concentrations for stations with similar coordinates to the sampling stations give POC inventory in the upper 100m ranging from 9.8 to 12 mmol C m^{-2} (Roca-Marti et al. 2016). Resulting POC export fluxes are 0.47 ± 0.05 mmol C m^{-2} d^{-1} at ST-30 and 0.23 ± 0.01 mmol C m^{-2} d^{-1} at ST-43. These fluxes are within range of ^{210}Po-derived POC fluxes reported by Roca-Marti et al. (2016). The POC export fluxes measured in the euphotic zones of the Chukchi Sea and across the Western Arctic using ^{210}Po/^{210}Pb disequilibrium in 2010 ranged from 109 to 1848 mmol C m^{-2} y^{-1} (~ 0.3 to 5 mmol C m^{-2} d^{-1}), with lower export fluxes found at

higher latitudes (He et al. 2015). The POC export flux at ST-43 is similar to previous reports in the Canada Basin of 0.30-0.35 mmol C m^{-2} d^{-1} (82°N, 169°W) (He et al. 2015).

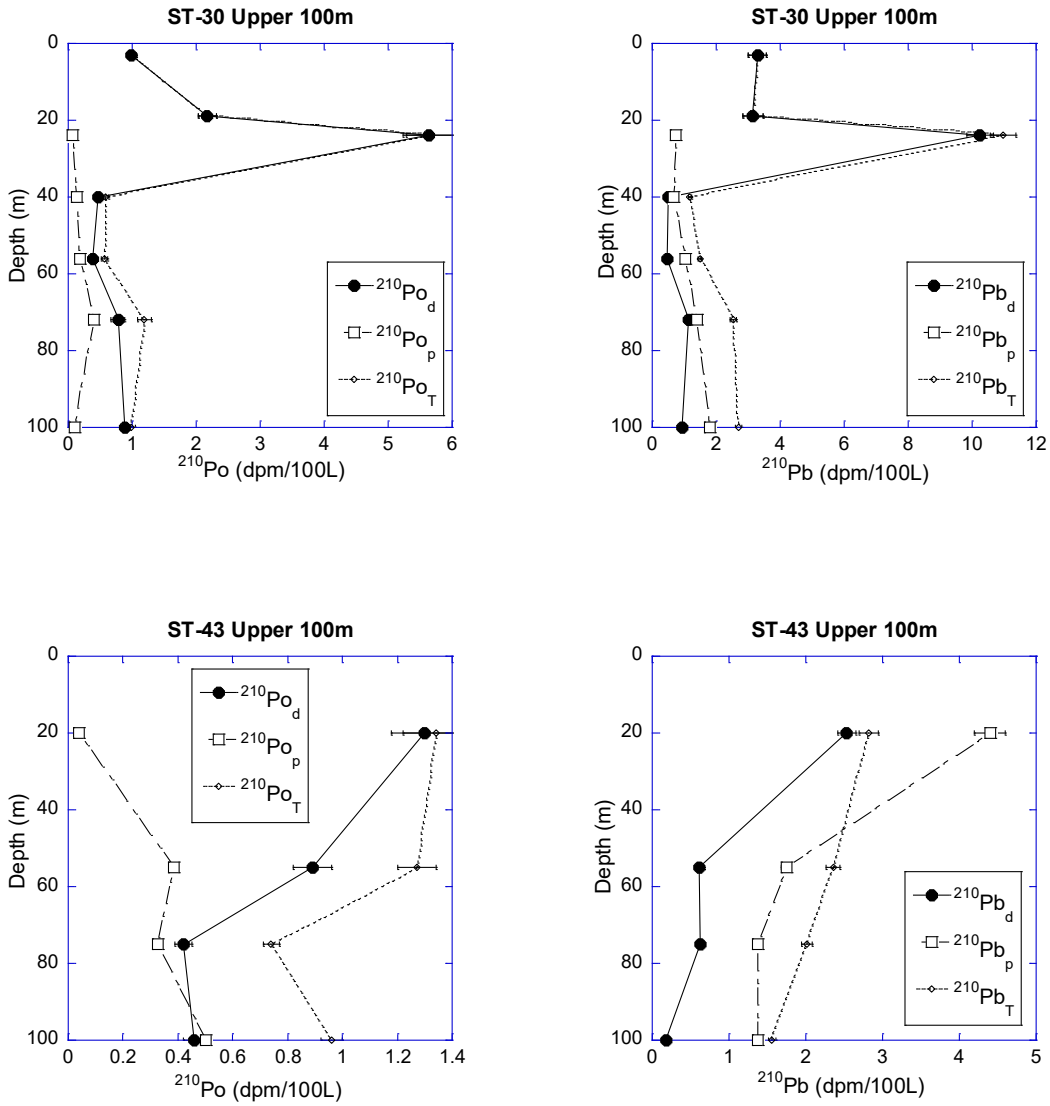

Figure 18. Activity profiles in upper 100m of ST-30 and ST-43.

CHAPTER 4

CONCLUSIONS

The results of this study lead to the following conclusions:

1. Disequilibrium between ^{210}Po and ^{210}Pb was observed from the measured activities of ^{210}Po and ^{210}Pb in IRS. The specific activities of ^{210}Pb in the interior IRS were about one to two orders of magnitude higher than that of benthic sediments. From the measured ^{210}Po/^{210}Pb activity ratios, the calculated average model-based residence time of ^{210}Pb in IRS was found to be 88 days. Assuming that ice-rafted sediments remain as a closed system after the incorporation of ^{210}Pb within sea ice, and it is transported subsequently, we calculated the transport velocity of IRS, which was consistent with satellite data for near-shelf IRS, but interior sediments seem to indicate a faster transport velocity. Possible explanations for this could include: 1) extreme temporal and directional variability within the transpolar drift stream; 2) the recent strengthening of Arctic drift streams within the last decade due to the polarity of the Arctic Oscillation; and/or 3) the loss of ^{210}Po and ^{210}Pb by leaching to meltwaters during the melt season, which would under estimate the residence time of these samples.
2. There was an observed disequilibrium between ^{210}Po and ^{210}Pb activities in ice floes throughout the ice cores sampled. From this disequilibrium, model-derived accumulation rates were obtained. The model-derived accumulation rates of 0.08 to 7.0 cm/d (mean – 1.4 cm/d) are in agreement with earlier studies. Additional data including stable isotopes and pigment data could be useful to gain better insight on the mechanisms of ice accumulation and ablation of sea ice.

3. The ^{210}Po and ^{210}Pb activities measured in snow samples are much higher than melt pond and surface seawater samples, most likely from accumulation from wet deposition events in the Arctic. Melt pond waters also exhibited higher activities relative to under ice seawater indicating the enrichment of melt pond water from snow melt during the melt season.
4. There is a gross disequilibrium between the total ^{210}Po and ^{210}Pb throughout the water column in the central Arctic basins, suggesting an early summer export event, and consistent with observations during the 2012 sea-ice minimum. A synthesis of all the published data on ^{210}Po and ^{210}Pb from the Arctic Ocean indicates that the particle concentration and particle flux seem to play a major role in the removal of particle-reactive radionuclides.
5. The residence time of ^{210}Pb in the Makarov Basin seems to be the highest, compared to all other published data from the Arctic Ocean.
6. From the measured activities of ^{210}Po and ^{210}Pb in aerosols, we estimated the depositional fluxes of ^{210}Pb. The depositional flux values calculated seem to agree quite well with the compiled data for the Arctic Ocean.

Overall, this study has provided a large, comprehensive dataset including many data that have never before been collected. The future utility of this work extends as far as the utility of the ^{210}Po/^{210}Pb pair encompasses as a tracer of environmental processes and a dating method for sub-annual processes, and will provide insight on the dynamics of ice floes, lithogenic and biogenic particles in the Arctic, as well as its overall biogeochemistry with respect to particle reactive elements. Further research should be conducted on IRS samples to 1) determine the mechanism of how enrichment of ^{210}Pb takes place in sea ice and whether

its incorporation of ^{210}Pb takes place in a single or multiple melt-freeze cycles; 2) heterogeneity in the activities of ^{210}Pb and $^{210}Po/^{210}Pb$ activity ratio in IRS collected from a single flow from a smaller region (less than 100 m^2 area); 3) estimate the accumulation and transport of contaminants by IRS measured via further analysis of sediment samples and through working with collaborators responsible for relevant parameters. Furthermore, the combined ice station data will be correlated with other significant parameters once this data is available (trace metals, micronutrients) in order to better establish the distribution of such elements and the biogeochemistry of surface ice and surface seawater.

APPENDIX A

Deployment information and activities measured in aerosol samples.

Deploy-	Deployment Start			Deployment End			Volume	^{210}Po	^{210}Pb	^{210}Po/^{210}Pb	^{210}Pb Flux	^{210}Po Flux
ment #	Date	Lat. (N)	Long. (W)	Date	Lat. (N)	Long. (W)	m^3	dpm $100m^{-3}$	dpm $100m^{-3}$	AR	dpm cm^{-2} y^{-1}	dpm cm^{-2} y^{-1}
1	8/10/2015	56.0743	170.509	8/17/2015	69.9257	167.6877	463.3	0042±0.0003	0.056±0.003	0.074±0.007	0.018±0.001	0.0013±0.0001
2	8/20/2015	75.5665	170.7498	8/23/2015	79.9968	174.9528	173.5	0.023±0.001	0.42±0.01	0.054±0.004	0.133±0.004	0.0071±0.0004
3	8/23/2015	80.0018	174.9595	8/27/2015	83.5722	-174.7305	274.8	0.033±0.002	0.63±0.03	0.052±0.004	0.20±0.01	0.0103±0.0006
4	8/27/2015	83.7577	-175.043	8/30/2015	86.2438	-170.6542	118.2	0.049±0.004	0.64±0.02	0.077±0.007	0.20±0.01	0.0156±0.0012
5	8/30/2015	86.3617	-171.6882	9/4/2015	88.3993	-176.6365	12.6	0.12±0.01	1.24±0.07	0.097±0.010	0.39±0.02	0.0379±0.0031
6	9/4/2015	88.4088	-176.7522	9/8/2015	89.9447	97.8478	271.7	0.029±0.002	0.63±0.02	0.046±0.004	0.20±0.01	0.0090±0.0006
7	9/8/2015	89.9413	104.19	9/12/2015	87.3515	149.4303	116.2	0.012±0.001	0.63±0.02	0.019±0.002	0.20±0.01	0.0037±0.0003
8	9/12/2015	87.2708	149.0443	9/16/2015	85.145	149.8545	72.3	0.0010 ± 0.00	0.34±0.02	0.0030±0.000	0.11±0.01	0.0003±0.0000
9	9/17/2015	85.1632	150.3953	9/20/2015	82.2587	149.3772	108.1	0.00039 ± 0.0	0.43±0.02	0.0090±0.000	0.14±0.01	0.0012±0.0001
10	9/21/2015	82.1005	150.811	9/26/2015	78.9737	148.501	320	0.0085±0.000	0.60±0.02	0.014±0.001	0.19±0.01	0.0027±0.0002
11	9/26/2015	78.8035	148.0932	9/29/2015	75.0467	150.1755	115.6	0.035±0.003	2.15±0.08	0.016±0.001	0.68±0.03	0.0110±0.0008
12	9/29/2015	75.0602	150.2147	10/3/2015	73.426	156.7932	211.4	0.028±0.002	0.75±0.03	0.037±0.003	0.24±0.01	0.0088±0.0006
13	10/3/2015	73.3972	156.7658	10/7/2015	71.9983	162.5618	150.8	0.031±0.002	0.95±0.04	0.033±0.003	0.30±0.01	0.0098±0.0007
14	10/7/2015	72.0043	162.5603	10/9/2015	65.9503	168.4485	90.2	0.055±0.004	0.76±0.05	0.073±0.007	0.24±0.02	0.0175±0.0011
									Average:	0.043±0.004	0.23±0.01	0.0097±0.0007

APPENDIX B

Activities and activity ratio measured in ice-rafted sediments.

ST #	Lat.	Long.	^{210}Po	^{210}Pb	^{210}Pb$_{xs}$*	(^{210}Po/^{210}Pb)$_T$	(^{210}Po/^{210}Pb)$_{xs}$	<^{7}Be>	<^{137}Cs>	<^{234}Th>
			dpm/g	dpm/g	dpm/g	AR	AR	dpm/g	dpm/g	dpm/g
E6195	87 45.1 N	179 43.429 W	60.2±1.9	122±3	121±3	0.49±0.02	0.49±0.02	11.9±1.1	BDL	BDL
			78.2±2.5	186±6	185±6	0.42±0.02	0.42±0.02			
			75.4±2.8	192±6	191±6	0.39±0.02	0.39±0.02			
E6244	88 58.393 N	150 24.788 W	12.3±0.4	40.3±1.8	39.3±1.9	0.30±0.02	0.29±0.02	0.147 ±0.003	BDL	BDL
			16.8±0.7	38.4±1.2	37.4±1.2	0.44±0.02	0.42±0.02			
			6.88±0.26	21.4±0.7	20.4±0.7	0.32±0.02	0.29±0.02			
GERIRS 1	84 31.40 N	116 11.43 E	2.86±0.11	4.93±0.19	3.11±0.28	0.58±0.03	0.33±0.08	BDL	BDL	BDL
			3.46±0.12	4.88±0.17	3.07±0.26	0.71±0.04	0.54±0.09			
			4.24±0.15	3.41±0.13	1.59±0.24	1.24±0.06	1.52±0.28			
GERIRS 2	84 51.64 N	124 11.69 E	0.82±0.03	2.27±0.09	0.45±0.22	0.36±0.02	-2.23±1.19	BDL	BDL	BDL
			1.31±0.05	2.25±0.10	0.43±0.22	0.58±0.03	-1.16±0.77			
			1.18±0.05	2.48±0.11	0.67±0.23	0.47±0.03	-0.96±0.46			

BDL = below detection level; *^{210}Pb$_{xs}$ determined using measured <^{226}Ra> activities of 1.02 ± 0.25 and 1.82 ± 0.20 dpm/g for E6195/E6244 and GERIRS 1/GERIRS 2, respectively.

APPENDIX C

Dissolved, particulate, total activities and activity ratios for ice station samples.

ST #	Ice Core Depth (cm)	$^{210}Po_p$ dpm 100L^{-1}	$^{210}Po_d$ dpm 100L^{-1}	$^{210}Po_T$ dpm 100L^{-1}	$^{210}Pb_p$ dpm 100L^{-1}	$^{210}Pb_d$ dpm 100L^{-1}	$^{210}Pb_T$ dpm 100L^{-1}	$^{210}Po_T/^{210}Pb_T$ AR
88°N 176°W								
31	**Snow**	220 ± 7	103 ± 3	323 ± 7	265 ± 9	1394 ± 51	1659 ± 52	0.20 ± 0.01
	0-20	20.9 ± 1.0	60.0 ± 2.2	80.9 ± 2.4	28.0 ± 1.1	174 ± 6	202 ± 6	0.40 ± 0.02
	20-40	5.59 ± 0.39	10.9 ± 0.6	16.4 ± 0.7	13.7 ± 0.6	72.1 ± 2.9	85.8 ± 3.0	0.19 ± 0.01
	40-60	1.36 ± 0.11	2.55 ± 0.19	3.91 ± 0.22	3.23 ± 0.20	11.9 ± 0.6	15.2 ± 0.6	0.26 ± 0.02
	60-80	1.89 ± 0.16	5.21 ± 0.34	7.10 ± 0.37	1.24 ± 0.08	6.23 ± 0.41	7.47 ± 0.41	0.95 ± 0.07
	80-100	1.04 ± 0.10	1.72 ± 0.13	2.75 ± 0.16	BDL	3.52 ± 0.25	3.52 ± 0.25	0.78 ± 0.07
	100-130	0.94 ± 0.09	2.70 ± 0.20	3.63 ± 0.22	0.031 ± 0.002	1.09 ± 0.09	1.12 ± 0.09	3.25 ± 0.32
	Under-ice	0.16 ± 0.02	1.26 ± 0.10	1.43 ± 0.10	0.14 ± 0.01	5.20 ± 0.22	5.34 ± 0.22	0.27 ± 0.02
89°N 89°E								
33	**Snow**	15.2 ± 0.5	112 ± 3	127 ± 3	78.4 ± 3.0	872 ± 32	951 ± 32	0.13 ± 0.01
	Melt pond	1.88 ± 0.09	9.35 ± 0.41	11.2 ± 0.4	5.62 ± 0.24	18.9 ± 0.7	24.6 ± 0.8	0.46 ± 0.02
	0-28	17.4 ± 0.8	13.7 ± 0.6	31.1 ± 1.0	37.1 ± 1.4	49.8 ± 1.9	86.9 ± 2.4	0.36 ± 0.01
	28-56	3.23 ± 0.22	40.2 ± 1.8	43.5 ± 1.8	2.09 ± 0.14	45.3 ± 1.8	47.4 ± 1.8	0.92 ± 0.05
	56-84	2.33 ± 0.15	1.52 ± 0.11	3.85 ± 0. 0.19	2.15 ± 0.14	6.09 ± 0.38	8.24 ± 0.41	0.47 ± 0.03
	84-112	0.25 ± 0.02	1.23 ± 0.10	1.48 ± 0.10	BDL	0.32 ± 0.03	0.32 ± 0.03	4.58 ± 0.51
	112-140	0.84 ± 0.07	3.60 ± 0.21	4.44 ± 0.23	1.11 ± 0.08	16.7 ± 0.8	17.8 ± 0.8	0.25 ± 0.02
	Under ice	0.041 ± 0.005	0.61 ± 0.10	0.65 ± 0.10	0.0009 ± 0.0001	3.79 ± 0.18	3.79 ± 0.18	0.17 ± 0.03
87°N 148°W								
39	**Snow**	2.85 ± 0.13	3.31 ± 0.12	6.16 ± 0.17	33.9 ± 1.3	158 ± 5	192 ± 5	0.032 ± 0.001
	Melt pond	0.90 ± 0.06	20.3 ± 0.8	21.2 ± 0.8	0.92 ± 0.06	60.1 ± 2.5	61.0 ± 2.5	0.35 ± 0.02
	0-38	44.8 ± 3.7	96.3 ± 3.3	141 ± 4	48.2 ± 1.7	0.78 ± 0.13	49.0 ± 1.7	2.88 ± 0.12
	38-76	3.67 ± 0.22	20.5 ± 0.9	24.2 ± 0.9	15.7 ± 0.7	59.7 ± 2.5	75.4 ±2.6	0.32 ± 0.02
	76-114	2.67 ± 0.17	9.97 ±0.47	12.6 ± 0.5	4.26 ± 0.21	72.7 ± 2.8	77.0 ± 2.8	0.16 ± 0.01
	114-152	2.70 ± 0.23	5.10 ±0.33	7.81 ± 0.41	7.03 ± 0.43	25.1 ± 1.5	32.1 ±1.5	0.24 ± 0.02
	152-190	3.99 ± 0.25	7.64 ±0.47	11.6 ± 0.5	10.7 ± 0.75	20.2 ± 0.9	31.0 ± 1.2	0.38 ± 0.02
	Under ice	0.074 ± 0.008	1.34 ± 0.18	1.41 ± 0.18	0.0087 ± 0.0007	12.5 ± 0.5	12.5 ± 0.5	0.11 ± 0.01
85°N 150°W								
42	**Snow**	8.89 ± 0.35	21.9 ± 0.8	30.8 ± 0.9	38.6 ± 1.5	238 ± 8	276 ± 8	0.11 ± 0.01
	Melt pond	1.48 ± 0.09	18.5 ± 0.8	19.9 ± 0.8	3.46 ± 0.18	59.7 ± 2.1	63.2 ± 2.1	0.32 ± 0.02
	0-20	4.46 ± 0.29	10.7 ± 0.6	15.1 ± 0.7	36.6 ± 1.9	94.2 ± 4.1	131 ± 5	0.12 ± 0.01
	20-40	7.37 ± 0.49	6.63 ± 0.44	14.0 ± 0.7	20.0 ± 1.0	30.9 ± 1.5	50.9 ± 1.8	0.28 ± 0.02
	40—60	14.1 ± 0.8	10.8 ± 0.6	24.9 ± 0.9	24.4 ± 1.1	34.7 ± 1.7	59.2 ± 2.0	0.42 ± 0.02
	60-80	4.51 ± 0.37	3.37 ± 0.27	7.88 ± 0.46	5.28 ± 0.35	16.8 ± 1.0	22.0 ± 1.1	0.36 ± 0.03
	80-100	2.64 ± 0.23	4.74 ± 0.33	7.38 ± 0.41	6.22 ± 0.44	28.1 ± 1.8	34.3 ± 1.8	0.21 ± 0.02
	Under ice	0.14 ± 0.01	1.31 ± 0.19	1.45 ± 0.19	0.38 ± 0.03	7.09 ± 0.28	7.47 ± 0.29	0.19 ± 0.03
85°N 149°W								
43	**Snow**	13.1 ± 0.5	23.4 ± 0.9	36.6 ± 1.0	27.1 ± 1.0	553 ± 19	580 ± 19	0.063 ± 0.003
	Melt pond	0.40 ± 0.03	61.0 ± 3.1	61.4 ± 3.1	0.28 ± 0.03	204 ± 7	205 ± 7	0.30 ± 0.02
	0-33	74.7 ± 3.2	37.2 ± 1.8	112 ± 4	120 ± 5	99.3 ± 3.5	219 ± 6	0.51 ± 0.02
	33-66	7.43 ± 0.39	12.2 ± 0.7	19.6 ± 0.8	14.3 ± 0.7	26.7 ± 1.4	41.0 ± 1.5	0.48 ± 0.03
	66-99	2.10 ± 0.16	8.15 ± 0.41	10.2 ± 0.4	6.50 ± 0.39	46.3 ± 1.7	52.8 ± 1.7	0.19 ± 0.01
	99-132	0.97 ± 0.08	1.37 ± 0.12	2.34 ± 0.14	0.13 ± 0.01	3.52 ± 0.24	3.65 ± 0.24	0.64 ± 0.06
	132-165	1.58 ± 0.12	4.48 ± 0.28	6.06 ± 0.30	1.64 ± 0.12	16.8 ± 1.9	18.4 ± 1.9	0.33 ± 0.04
	Under ice	0.11 ± 0.01	1.48 ± 0.24	1.58 ± 0.24	0.37 ± 0.03	6.04 ± 0.26	6.41 ± 0.26	0.25 ± 0.04
82°N 149°W								
46	**Snow**	2.42 ± 0.11	7.40 ± 0.35	9.82 ± 0.36	5.64 ± 0.23	469 ± 18	475 ± 17	0.021 ± 0.001
	Melt pond	4.02 ± 0.16	22.6 ± 1.0	26.6 ± 1.0	2.70 ± 0.11	112 ± 5	115 ± 5	0.23 ± 0.01
	0-34	5.71 ± 0.34	18.1 ± 0.8	23.8 ± 0.9	10.7 ± 0.6	50.9 ± 2.0	61.5 ± 2.1	0.39 ± 0.02
	34-68	2.36 ± 0.18	5.53 ± 0.37	7.89 ± 0.41	5.78 ± 0.36	15.9 ± 1.7	21.6 ± 1.8	0.36 ± 0.04
	68-102	0.37 ± 0.03	3.21 ± 0.24	3.57 ± 0.24	1.96 ± 0.15	11.9 ± 0.8	13.8 ± 0.8	0.26 ± 0.02
	102-136	0.26 ± 0.03	1.73 ± 0.16	1.99 ± 0.16	0.011 ± 0.001	7.80 ± 0.66	7.81 ± 0.66	0.25 ± 0.03
	136-170	0.53 ± 0.04	2.35 ± 0.18	2.88 ± 0.19	0.87 ± 0.07	7.26 ± 0.45	8.13 ± 0.45	0.35 ± 0.03
	Under ice	0.34 ± 0.03	9.89 ± 0.45	10.2 ± 0.4	0.42 ± 0.03	19.2 ± 0.7	19.6 ± 0.7	0.52 ± 0.03

BDL = below detection level; activity of sample was lower than the average blank level

APPENDIX D

Dissolved, particulate, total activities and activity ratios for ST-30 and ST-43.

ST #	Depth	$^{210}Po_p$		$^{210}Po_d$	$^{210}Po_T$	$^{210}Pb_p$		$^{210}Pb_d$	$^{210}Pb_T$	$^{210}Po_T/^{210}Pb_T$
	(m)	dpm 100L^{-1}		dpm 100L^{-1}	dpm 100L^{-1}	dpm 100L^{-1}		dpm 100L^{-1}	dpm 100L^{-1}	AR
87°N 179°W		<51µm	>51 µm			<51 µm	>51 µm			
30	3	NM	NM	0.99 ± 0.08	0.99 ± 0.08	NM	NM	3.28 ± 0.28	3.28 ± 0.28	0.30 ± 0.03
	19	NM	NM	2.17 ± 0.14	2.17 ± 0.14	NM	NM	3.15 ± 0.31	3.15 ± 0.31	0.69 ± 0.08
	24	BDL	0.061 ± 0.003	5.63 ± 0.40	5.69 ± 0.40	0.45 ± 0.02	0.28 ± 0.01	10.2 ± 0.41	11.0 ± 0.4	0.52 ± 0.04
	40	0.076 ± 0.004	0.052 ± 0.002	0.46 ± 0.05	0.59 ± 0.05	0.49 ± 0.03	0.18 ± 0.01	0.52 ± 0.03	1.18 ± 0.05	0.50 ± 0.05
	56	0.16 ± 0.01	0.029 ± 0.002	0.38 ± 0.05	0.57 ± 0.05	0.94 ± 0.04	0.091 ± 0.004	0.47 ± 0.03	1.50 ± 0.05	0.38 ± 0.03
	72	0.37 ± 0.01	0.036 ± 0.001	0.78 ± 0.11	1.19 ± 0.11	1.28 ± 0.05	0.12 ± 0.01	1.14 ± 0.08	2.54 ± 0.09	0.47 ± 0.05
	100	0.053 ± 0.002	0.050 ± 0.002	0.88 ± 0.06	0.99 ± 0.06	1.66 ± 0.07	0.14 ± 0.01	0.92 ± 0.06	2.71 ± 0.10	0.36 ± 0.02
	125	0.033 ± 0.001	0.024 ± 0.001	0.41 ± 0.05	0.46 ± 0.05	1.10 ± 0.06	0.060 ± 0.003	1.01 ± 0.07	2.17 ± 0.09	0.21 ± 0.02
	175	0.25 ± 0.01	0.057 ± 0.002	1.39 ± 0.09	1.69 ± 0.09	0.79 ± 0.03	0.18 ± 0.01	3.05 ± 0.21	4.02 ± 0.21	0.42 ± 0.03
	225	0.44 ± 0.02	0.078 ± 0.003	1.03 ± 0.11	1.55 ± 0.11	0.94 ± 0.07	0.17 ± 0.01	1.90 ± 0.11	3.02 ± 0.13	0.51 ± 0.04
	229	0.32 ± 0.01	0.078 ± 0.003	NM	NM	1.15 ± 0.06	0.20 ± 0.01	NM	NM	NM
	260	0.46 ± 0.02	0.094 ± 0.004	0.77 ± 0.07	1.32 ± 0.07	1.14 ± 0.05	0.20 ± 0.01	1.52 ± 0.08	2.86 ± 0.10	0.46 ± 0.03
	375	BDL	0.14 ± 0.005	1.52 ± 0.10	1.66 ± 0.10	2.84 ± 0.13	0.30 ± 0.01	2.23 ± 0.13	5.38 ± 0.19	0.31 ± 0.02
	500	0.83 ± 0.03	NM	1.40 ± 0.08	2.24 ± 0.09	3.24 ± 0.19	NM	2.46 ± 0.22	5.70 ± 0.29	0.39 ± 0.03
	800	BDL	0.14 ± 0.01	2.38 ± 0.12	2.52 ± 0.12	6.05 ± 0.29	0.26 ± 0.01	6.67 ± 0.47	13.0 ± 0.6	0.19 ± 0.01
	1000	1.11 ± 0.04	BDL	3.56 ± 0.16	4.67 ± 0.16	2.04 ± 0.09	1.43 ± 0.31	10.8 ± 0.5	14.2 ± 0.6	0.33 ± 0.02
	1400	1.55 ± 0.06	0.20 ± 0.01	2.39 ± 0.12	4.14 ± 0.12	1.74 ± 0.07	0.32 ± 0.02	6.42 ± 0.34	8.48 ± 0.35	0.49 ± 0.03
	1650	NM	NM	2.96 ± 0.15	2.96 ± 0.15	NM	NM	2.80 ± 0.19	2.80 ± 0.19	1.06 ± 0.09
	1891	2.35 ± 0.07	0.36 ± 0.02	NM	NM	1.74 ± 0.08	0.40 ± 0.02	NM	NM	NM
	1900	2.49 ± 0.09	0.36 ± 0.02	2.52 ± 0.13	5.37 ± 0.16	2.12 ± 0.09	0.43 ± 0.02	5.77 ± 0.25	8.31 ± 0.27	0.65 ± 0.03
	2400	2.78 ± 0.10	0.34 ± 0.01	3.35 ± 0.14	6.47 ± 0.18	2.20 ± 0.08	0.32 ± 0.01	7.96 ± 0.52	10.5 ± 0.5	0.62 ± 0.04
	2900	3.08 ± 0.12	0.49 ± 0.02	3.61 ± 0.15	7.18 ± 0.20	1.74 ± 0.08	0.41 ± 0.02	10.4 ± 0.4	12.6 ± 0.4	0.57 ± 0.03
	3400	4.86 ± 0.15	0.68 ± 0.02	3.31 ± 0.14	8.84 ± 0.21	3.24 ± 0.12	0.62 ± 0.02	11.0 ± 0.9	14.9 ± 0.9	0.59 ± 0.04
	3800	4.56 ± 0.17	0.92 ± 0.04	4.32 ± 0.17	9.81 ± 0.24	3.52 ± 0.13	0.80 ± 0.03	17.2 ± 2.6	21.5 ± 2.6	0.46 ± 0.06
	3875	5.10 ± 0.19	0.80 ± 0.03	3.89 ± 0.16	9.79 ± 0.25	3.51 ± 0.10	0.66 ± 0.02	11.7 ± 0.6	15.9 ± 0.6	0.62 ± 0.03
	3925	6.72 ± 0.25	0.83 ± 0.03	3.27 ± 0.14	10.8 ± 0.3	BDL	0.73 ± 0.03	13.1 ± 0.8	13.8 ± 0.8	0.78 ± 0.05
85°N 149°W										
43	20	BDL	0.040 ± 0.002	1.30 ± 0.12	1.34 ± 0.12	4.12 ± 0.20	0.28 ± 0.01	2.53 ± 0.12	2.82 ± 0.12	0.48 ± 0.05
	55	0.37 ± 0.02	0.016 ± 0.001	0.89 ± 0.07	1.27 ± 0.07	1.69 ± 0.07	0.054 ± 0.004	0.62 ± 0.06	2.36 ± 0.09	0.54 ± 0.04
	75	0.29 ± 0.01	0.034 ± 0.002	0.42 ± 0.03	0.74 ± 0.03	1.27 ± 0.05	0.11 ± 0.01	0.63 ± 0.04	2.01 ± 0.07	0.37 ± 0.02
	100	0.46 ± 0.02	0.041 ± 0.002	0.46 ± 0.04	0.96 ± 0.04	1.23 ± 0.05	0.15 ± 0.01	0.18 ± 0.02	1.56 ± 0.05	0.61 ± 0.03
	140	0.16 ± 0.01	0.039 ± 0.002	0.29 ± 0.03	0.49 ± 0.03	1.27 ± 0.05	0.10 ± 0.00	0.30 ± 0.03	1.67 ± 0.06	0.29 ± 0.02
	225	0.38 ± 0.01	0.062 ± 0.003	1.75 ± 0.09	2.19 ± 0.09	1.13 ± 0.04	0.21 ± 0.01	0.92 ± 0.08	2.27 ± 0.09	0.96 ± 0.06
	330	0.56 ± 0.02	0.081 ± 0.005	1.54 ± 0.08	2.19 ± 0.08	1.37 ± 0.05	0.21 ± 0.01	2.90 ± 0.15	4.48 ± 0.15	0.49 ± 0.02
	500	1.37 ± 0.06	0.11 ± 0.00	1.20 ± 0.08	2.69 ± 0.10	1.82 ± 0.06	0.27 ± 0.01	1.91 ± 0.26	4.00 ± 0.26	0.67 ± 0.05
	600	1.22 ± 0.04	0.13 ± 0.01	1.71 ± 0.10	3.06 ± 0.10	1.92 ± 0.09	0.21 ± 0.01	3.75 ± 0.23	5.88 ± 0.25	0.52 ± 0.03
	850	1.19 ± 0.04	0.16 ± 0.01	15.3 ± 0.74	16.6 ± 0.74	2.08 ± 0.10	0.23 ± 0.01	30.2 ± 1.2	32.5 ± 1.22	0.51 ± 0.03
	1000	1.17 ± 0.05	0.15 ± 0.01	1.99 ± 0.10	3.31 ± 0.11	2.09 ± 0.11	0.22 ± 0.01	4.78 ± 0.41	7.10 ± 0.43	0.47 ± 0.03
	1400	1.32 ± 0.05	0.17 ± 0.01	2.88 ± 0.13	4.37 ± 0.13	1.42 ± 0.06	0.20 ± 0.01	4.74 ± 0.51	6.35 ± 0.52	0.69 ± 0.06
	1800	1.70 ± 0.06	0.20 ± 0.01	2.31 ± 0.10	4.21 ± 0.11	1.28 ± 0.08	0.24 ± 0.01	6.17 ± 0.26	7.68 ± 0.27	0.55 ± 0.02
	2000	1.77 ± 0.07	0.32 ± 0.02	2.17 ± 0.11	4.25 ± 0.13	1.56 ± 0.06	0.46 ± 0.02	3.59 ± 0.18	5.61 ± 0.19	0.76 ± 0.03
	2100	NM	NM	2.05 ± 0.11	2.05 ± 0.11	NM	NM	5.23 ± 0.69	5.23 ± 0.69	0.39 ± 0.06
	2125	1.68 ± 0.07	0.45 ± 0.02	2.28 ± 0.12	4.41 ± 0.14	2.65 ± 0.10	0.81 ± 0.04	4.71 ± 0.43	8.18 ± 0.45	0.54 ± 0.03
	2166	2.04 ± 0.08	0.59 ± 0.02	NM	NM	2.34 ± 0.08	0.96 ± 0.04	NM	NM	NM

NM = not measured
BDL = below detection level; activity of sample was lower than the average blank level
For both ^{210}Po and ^{210}Pb, when no particulate data available, total activity = dissolved activity is assumed

REFERENCES

Aagaard, K., Swift, J.H., and E.C. Carmack. 1985. Thermohaline circulation in the arctic Mediterranean seas. Journal of Geophysical Research 90: 4833-4846.

Alexandrov, D.V., Jouzel, J., Nizovtseva, I., and L.B. Ryashko. 2013. Review Article: the false-bottom ice. The Cryosphere Discussion 7: 5659-5682.

"Arctic Sea Ice Minimum." Global Climate Change. Ed. Holly Shaftel. Earth Science Communications Team at NASA's Jet Propulsion Laboratory, n.d. Web. 7 July 2017.

Arrigo, K. R., and G. L. van Dijken. 2015. Continued increases in Arctic Ocean primary production. Progress in Oceanography 136: 60–70.

Bacon, M.P., Huh, C.A., and R.M. Moore. 1989. Vertical profiles of some natural radionuclides over the Alpha Ridge, Arctic Ocean. Earth and Planetary Science Letters 95: 15-22.

Baskaran, M., Swarzenski, P.W., and D. Porcelli. 2003. Role of colloidal material in the removal of ^{234}Th in the Canada Basin of the Arctic Ocean. Deep-Sea Research I 50: 1353-1373.

Baskaran, M. 2005. Interaction of sea ice sediments and surface sea water in the Arctic Ocean: Evidence from excess ^{210}Pb. Geophysical Research Letters 32: L12601.

Baskaran, M. 2011. Handbook of environmental isotope geochemistry. Springer, Heidelberg [Germany]; New York.

Baskaran, M., Church, T.M., Hong, G.H., Kumar, A., Qiang, M., Choi, H., Rigaud, S., and K. Maiti. 2013. Effects of flow rates and composition of the filter, and decay-in-growth correction factors involved with the determination of in-situ particulate ^{210}Po and ^{210}Pb in seawater. Limnology and Oceanography (Methods) 11: 126-138.

Buesseler, K.O., Bacon, M.P., Cochran, J.K., and H.D. Livingston. 1992. Carbon and nitrogen export during the JGOFS North Atlantic Bloom Experiment estimated from 234Th: 238U disequilibria. Deep-Sea Research 39: 1115–1137.

Cai, P., Rutgers van der Loeff, M.M., Stimac, I., Nöthig, E.-M., Lepore, K. and S. B. Moran. 2010. Low export flux of particulate organic carbon in the central Arctic Ocean as revealed by 234Th:238U disequilibrium. Journal of Geophysical Research 115: C10037.

Cherepanov, N.V., Nazintsev, I.L, and K.P. Tyshko. 1989. Contact supercooling of water layers and bottom ice formation in the sea in Electro Physical and Physical-Mechanical Properties of Ice, edited by: Bogordskii, V.V. and V.P. Vavrilo, Gidrometeoizdat, St. Petersburg, pp. 124-134.

Church, T.M., Rigaud, S., Baskaran, M., Friedrich, J., Masqué, P., Puigcorbe, V., Kim, G., Radakovitch, O., Hong, G.H., and G. Stewart. 2012. Intercalibration studies of ^{210}Po and ^{210}Pb in dissolved and particulate seawater samples. Limnology and Oceanography (Methods) 10: 776-789.

Clark, D.L. 1990. Arctic ocean ice cover: geologic history and climatic significance. In: A. Grantz, L. Johnson and J.F. Sweeney (eds), The Arctic Ocean Region. (The Geology of North America, L.) Geological Society of America, Boulder, CO, pp. 53-62.

Cochran, J.K., Hirschberg, D.J., Livingston, H.D., Buesseler, K.O., and R.M. Key. 1995. Natural and anthropogenic radionuclide distributions in the Nansen Basin, Arctic Ocean: scavenging rates and circulation time scales. Deep-Sea Research II 42: 1495–1517.

Cooper, L.W., Larsen, I.L, Beasley, T.M., Dolvin, S.S., Grebmeier, J.M., Kelley, J.M., Scott, M.R., and A. Johnson-Pyrtle. 1998. The distribution of radiocesium and plutonium in sea

ice-entrained Arctic sediments in relation to potential sources and sinks. Journal of Environmental Radioactivity 39: 279-303.

Cutter, G., Andersson, P., Codispoti, L., Croot, P., Francois, R., Lohan, M.C., Obata, H., and M. Rutgers v.d. Loeff. 2010. Sampling and Sample-handling Protocols for GEOTRACES Cruises, (Miscellaneous).

Darby, D.L., Burckle, L.H., and D.L. Clark. 1974. Airborne dust on the Arctic pack ice, its composition and fallout rate. Earth and Planetary Science Letters 24: 166-172.

Dethleff, D. 2005. Entrainment and export of Laptev Sea ice sediments, Siberian Arctic. Journal of Geophysical Research 110: C07009.

Eicken, H. 1994. Structure of under-ice melt ponds in the central Arctic and their effect on the sea-ice cover. Limnology and Oceanography 39: 682-694.

Eicken, H., Krouse, H.R., Kadko, D., and D.K. Perovich. 2002. Tracer studies of pathways and rates of meltwater transport through Arctic summer sea ice. Journal of Geophysical Research 107: 8046.

Eicken, H., Reimnitz, E., Alexandrov, V., Martin, T., Kassens, H., and T. Viehoff. 1997. Sea-ice processes in the Laptev Sea and their importance for sediment export. Continental Shelf Research 17: 205-233.

Faure, G. and T.M. Mensing. 2005. Isotopes: Principles and Applications. Hoboken, NJ: Wiley. Print.

Fernandez-Mendez, M., Katlein, C., Rabe, B., Nicolaus, M., Peeken, I., Bakker, K., Flores, H., and A. Boetius. 2015. Photosynthetic production in the central Arctic Ocean during the record sea-ice minimum in 2012. Biogeosciences 23: 3525-3549.

GEOTRACES: An international study of the marine biogeochemical cycles of trace elements and their isotopes. Science Plan. 2006. Scientific Committee on Oceanic Research (SCOR).

He, J., Yu, W., Lin, W., Men, W., and L. Chen. 2015. Particulate organic carbon fluxes on Chukchi Shelf, western Arctic Ocean, derived from $^{210}Po/^{210}Pb$ disequilibrium. Chinese Journal of Oceanology and Limnology 33: 741-747.

Hong, G.H., Baskaran, M., Church, T.M., and M. Conte. 2013. Scavenging, cycling and removal fluxes of ^{210}Po and ^{210}Pb at the Bermuda time-series study site. Deep-Sea Research II 93: 108-118.

International Atomic Energy Agency (IAEA). 1985. Sediment Kds and concentration factors for radionuclides in the marine environment. Technical Report 247, Vienna.

Kellogg, W.W. 1975. Climate feedback mechanisms involving the polar regions, in Climate of the Arctic, edited by G. Weller and S.A. Bowling, pp. 111-116, University of Alaska, Fairbanks.

Kwok, R., Spreen, G., and S. Pang. 2013. Arctic sea ice circulation and drift speed: Decadal trends and ocean currents. Journal of Geophysical Research 118: 2408-2425.

Lepore, K., Moran, S.B., Grebmeier, J.M., Cooper, L.W., Lalande, C., Maslowski, W., Hill, V., Bates, N.R., and D.A. Hansell. 2007. Seasonal and interannual changes in POC export and deposition in the Chukchi Sea. Journal of Geophysical Research 112: C10024.

Lepore, K., Moran, S.B., and J.N. Smith. 2009. ^{210}Pb as a tracer of shelf-basin transport and sediment focusing in the Chukchi Sea. Deep-Sea Research II 56: 1305-1315.

Masqué, P., Cochran, J.K., Hirschberg, D.J., Dethleff, D., Hebbeln, D., Winkler, A., and S. Pfirman. 2007. Radionuclides in Arctic sea ice: Tracers of sources, fates, and ice transit time scales. Deep-Sea Research I 54: 1289-1310.

Matisoff, G. and P.J. Whiting. 2011. Measuring soil erosion rates using natural (7Be, ^{210}Pb) and anthropogenic (137Cs, 239,240Pu) radionuclides. In: M. Baskaran (ed), Handbook of Environmental Isotope Geochemistry. Springer, Berlin, pp. 487-519.

Melling, H., and R.M. Moore. 1995. Modification of halocline source waters during freezing on the Beaufort Sea shelf: evidence from oxygen isotopes and dissolved nutrients. Continental Shelf Research 15: 89-113.

Moore, R.M., and J.N. Smith. 1986. Disequilibria between ^{226}Ra, ^{210}Pb and ^{210}Po in the Arctic Ocean and the implications for chemical modification of the Pacific water inflow. Earth and Planetary Science Letters 77: 285-292.

Moran, S. B., Ellis, K.M. and J. N. Smith. 1997. 234Th/238U disequilibrium in the central Arctic Ocean: Implications for particulate organic carbon export, Deep-Sea Research II 44: 1593–1606.

Moran, S.B., Kelly, R.P., Hagstrom, K., Smith, J.N., Grebmeier, J.M., Cooper, L.W., Cota, G.F., Walsh, J.J., Bates, N.R., Hansell, D.A., Maslowski, W., Nelson, R.P., and S. Mulsow. 2005. Seasonal changes in POC export flux in the Chukchi Sea and implications for water column-benthic coupling in Arctic shelves. Deep-Sea Research II 52: 3427-3451.

Moritz, R.E., and D.K. Perovich. 1996. Surface heat budget of the Arctic Ocean Science Plan, ARCSS/OAIII Rep. 5, 64 pp., University of Washington, Seattle.

Murray, J.W., Paul, B., Dunne, J.P., and T. Chapin. 2005. ^{234}Th, ^{210}Pb, ^{210}Po and stable Pb in the central equatorial Pacific: Tracers for particle cycling. Deep-Sea Research I 52: 2109-2139.

National Snow and Ice Data Center. Quick Facts on Arctic Sea Ice, National Snow and Ice Data Center. N.p., n.d. Web. 15 Jan. 2017.

Niedermiller, J., and M. Baskaran. N.d. Comparison of the scavenging intensity, remineralization and residence time of ^{210}Po and ^{210}Pb at key interfaces (biotic, sediment-water and hydrothermal) of the East Pacific GEOTRACES Transect. Marine Chemistry: in review.

Notz, D., McPhee, M.G., Worster, M.G., Maykut, G.A., Schlunzen, K.H., and H. Eicken. 2003. Impact of underwater-ice evolution on Arctic summer sea ice. Journal of Geophysical Research 108: 3223.

Nguyen, A.T., Menemenlis, D., and R. Kwok. 2009. Improved modeling of the Arctic halocline with a subgrid-scale brine rejection parameterization. Journal of Geophysical Research 114: C11014.

Nürnberg, D., Wollenburg, I., Dethleff, D., Eicken, H., Kassens, H., Letzig, T., Reimnitz, E., and J. Thiede. 1994. Sediments in Arctic sea ice – implications for entrainment, transport and release. Marine Geology 119: 185-214.

Peralta-Ferriz, C., and R. Woodgate. 2015. Seasonal and inter-annual variability of pan-Arctic surface mixed layer properties from 1979 to 2012 from hydrographic data. Progress in Oceanography 134: 19-53.

Perovich, D.K., Grenfell, T.C., Richter-Menge, J.A., Light, B., Tucker III, W.B., and H. Eicken. 2003. Thin and thinner: sea ice mass balance measurements during SHEBA. Journal of Geophysical Research 108: 8050.

Pfirman, S.L, Eicken, H., Bauch, D., and W.F. Weeks. 1995. The potential transport of pollutants by Arctic sea ice. Science of the Total Environment 159: 129-145.

Pfirman, S., Lange, M.A., Wollenburg, I., and P. Schlosser. 1990. Sea ice characteristics and the role of sediment inclusions in deep-sea deposition: Arctic-Antarctic comparisons. In: U. Bleil and J. Thiede (Eds), Geological History of the Polar Oceans: Arctic versus Antarctic. Kluwer Academic Publishers, pp. 187-211.

Pickart, R.S., Weingartner, T.J., Pratt, L.J., Zimmermann, S., and D.J. Torres. 2005. Flow of winter-transformed Pacific water into the Western Arctic. Deep-Sea Research II 52: 3175-3198.

Polashenski, C., Golden, K.M., Perovich, D.K., Skyllingstad, E., Arnsten, A., Stwertka, C., and N. Wright. 2016. Percolation blockage: the process that enables melt pond formation on first year Arctic sea ice, preprint, 49 pp.

Polashenski, C., Perovich, D., Richter-Menge, J., and B. Elder. 2011. Seasonal ice mass-balance buoys: adapting tools to the changing Arctic. Annals of Glaciology 52: 18-26.

Rigaud, S., Stewart, G., Baskaran, M., Marsan, D., and T. Church. 2015. ^{210}Po and ^{210}Pb distribution, dissolved-particulate exchange rates, and particulate export along the North Atlantic US GEOTRACES GA03 section. Deep-Sea Research II 116: 60-78.

Rigor, I.J., and Wallace, J.M. 2004. Variations in the age of Arctic sea-ice and summer sea-ice extent. Geophysical Research Letters 31: L09401.

Roca-Marti, M., Puigcorbe, V., Rutgers van der Loeff, M. M., Katlein, C., Fernandez-Mendez, M., Peeken, I., and P. Masqué. 2016. Carbon export fluxes and export efficiency in the central Arctic during the record sea-ice minimum in 2012: a joint ^{234}Th/^{238}U and ^{210}Po/^{210}Pb study. Journal of Geophysical Research: Oceans 121: 5030-5049.

Schlosser, P., Smith, J.H., Lewis, D., and S. Pfirman. 1995. The role of the large-scale Arctic Ocean circulation in the transport of contaminants. Deep-Sea Research II 42: 1341-1553.

Semertzidou, P., Piliposian, G.T., and P.G. Appleby. 2016. Atmospheric residence time of ^{210}Pb determined from the activity ratios with its daughter radionuclides ^{210}Bi and ^{210}Po. Journal of Environmental Radioactivity 160: 42-53.

Smith, J.N., and K.M. Ellis. 1995. Radionuclide tracer profiles at the CESAR Ice Station and Canadian Ice Island in the Western Arctic Ocean. Deep-Sea Research II 42: 1447-1470.

Smith, J.N., Moran, S.B., and R.W. Macdonald. 2003. Shelf-basin interactions in the Arctic Ocean based on ^{210}Pb and Ra isotope tracer distributions. Deep-Sea Research I 50: 397-416.

Stein, R. and R.W. Macdonald. 2004. The organic carbon cycle in the Arctic Ocean, first ed. Springer, Berlin.

Stewart, G., Cochran, J.K., Miquel, J.C., Masqué, P., Szlosek, J., Rodriguez y Baena, A.M., Folwer, S.W., Gasser, B., and D.J. Hirschberg. 2007. Comparing POC export from ^{234}Th/^{238}U and ^{210}Po/^{210}Pb disequilibria with estimates from sediment traps in the northwest Mediterranean. Deep-Sea Research I 54: 1549-1570.

Trimble, S.M., Baskaran, M., and D. Porcelli. 2004. Scavenging of thorium isotopes in the Canada Basin of the Arctic Ocean. Earth and Planetary Science Letters 222: 915-932.

Trimble, S.M., and M. Baskaran. 2005. The role of suspended particulate matter in ^{234}Th scavenging and ^{234}Th-derived export fluxes of POC in the Canada Basin of the Arctic Ocean. Marine Chemistry 96: 1-19.

Tucker, W. B., David Wallace Cate, and Vicki Keating. The 1994 Arctic Ocean Section: The First Major Scientific Crossing of the Arctic Ocean. Hanover, NH: U.S. Army Cold Regions Research and Engineering Laboratory, 1996. Print.

Tucker, W.B. III, Gow, A.J., Meese, D.A., and H.W. Bosworth. 1999. Physical characteristics of summer sea ice across the Arctic Ocean. Journal of Geophysical Research 104: 1489-1504.

Turekian, K.Y., Nozaki, Y. and Benninger, L.K., 1977. Geochemistry of atmospheric radon and radon products. Annual Review of Earth and Planetary Sciences, 5: 227.

Untersteiner, N. 1968. Natural desalination and equilibrium salinity profile of perennial sea ice. Journal of Geophysical Research 73: 1251-1257.

Untersteiner, N. and F. I. Badgley. 1958. Preliminary results of thermal budget studies on Arctic pack ice during summer and autumn. In Arctic Sea Ice, National Academy of Science, National Resource Council, Washington DC, pp. 85-92.

"US Arctic GEOTRACES: Cruise Report." GEOTRACES.org. N.p., 12 Oct. 2015. Web.Verdeny, E., Masqué, P., Garcia-Orellana, J., Hanfland, C., Cochran, J.K., and G. Stewart. 2009. POC export from ocean surface waters by means of $^{234}Th/^{238}U$ and $^{210}Po/^{210}Pb$ disequilibria: a comparison of two radiotracer pairs. Deep-Sea Research II 56: 1502-1518.

Verdeny, E., Masqué, P., Garcia-Orellana, J., Hanfland, Cl, Cochran, J.K., and G.M. Stewart. 2009. POC export from ocean surface waters by means of $^{234}Th/^{238}U$ and $^{210}Po/^{210}Pb$ disequilibria: A review of the use of two radiotracer pairs. Deep-Sea Research II 56: 1502-1518.

Weingartner, T., Cavalieri, D.J., Aagaard, K., and Y. Sasaki. 1998. Circulation, dense water formation, and outflow on the northeast Chukchi shelf. Journal of Geophysical Research 103: 7647-7661.

Yang, W., Guo, L., Chuang, C.Y., Schumann, D., Ayranov, M., and P.H. Santschi. 2013. Adsorption characteristics of ^{210}Pb, ^{210}Po and ^{7}Be onto micro-particle surfaces and the effects of macromolecular organic compounds Geochimica Et Cosmochimica Acta. 107: 47-64.

ABSTRACT

USING ^{210}Po/^{210}Pb DISEQUILIBRIA TO CHARACTERIZE THE BIOGEOCHEMISTRY AND QUANTIFY THE DYNAMICS OF SEA ICE IN THE ARCTIC

by

KATHERINE KRUPP

May 2017

Advisor: Dr. Mark Baskaran

Major: Geology

Degree: Master of Science

Understanding the biogeochemical cycles of the Arctic Ocean is highly significant due to its many unique characteristics which impact the cycling of important trace elements, isotopes, and nutrients. Furthermore, with its seasonally-changing sea ice extent and substantial role in the global radiation balance, the Arctic is considered a sensitive indicator of global change. The study of ^{210}Po and ^{210}Pb disequilibria is used to determine 1) the residence time of ice-rafted sediments in sea ice, 2) ice floe dynamics such as ice accumulation rates, and 3) biogeochemical characterization of the Arctic due to the natural occurrence and particle reactivity of ^{210}Po and ^{210}Pb. The "age" of ice-rafted sediments ranged from 56-136 days, and transport rates of 0.08 to 0.17 m/s were observed, consistent with previous reports, with the higher rates potentially influenced by non-conservative behavior of radionuclides during melt season. The mechanisms of isotopic disequilibria with depth in ice cores is not yet clearly understood, but model-based estimates of ice accumulation range from 0.08 – 7 cm/d (mean = 1.4 cm/d). Wide-scale ^{210}Po deficiency in water columns of the central and western Arctic (integrated AR's = 0.51± 0.07 and 0.56 ± 0.07 for ST-30 and ST-43, respectively) indicate early summer export of ^{210}Po with biogenic particles.

AUTOBIOGRAPHICAL STATEMENT

Katherine Krupp began to pursue an education in environmental sciences in 2011. Having an inherent love of nature, she felt that a formal education would be most fulfilling if focused on the science of the Earth, how humans depend on and affect the natural environment, and how to solve current environmental crises. She received an Associate Degree in General Studies in 2013 and a Bachelor of Science in Environmental Science in 2014. During her undergraduate education, Krupp began working for Dr. Mark Baskaran as a student assistant, where she developed and carried out an experiment to analyze the emanation of radon from a suite of natural minerals and as a function of physical and mineralogical properties. This work eventually led to a publication in American Mineralogist. From this experience, she caught the research "bug" and continued to work with Dr. Baskaran as a graduate research assistant, the result of which is contained in this thesis. When she is not in the lab, Krupp likes to spend time with her fiancé, Steve, and her pit bull, Dolly. They enjoy hiking, birding, playing music, and exploring the city of Detroit. Krupp is also an extensive hobbyist, with experience in the husbandry of rare freshwater fish of the family Cichlidae and various reptiles, and she keeps a wide variety of plant terrariums with species spanning from succulents and cacti to carnivorous bog plants and mosses.